2018

An integrated model for the probabilistic prediction of yield strength in electron-beam additively manufactured Ti-6Al-4V

Thomas Kiel Ales
Iowa State University

An integrated model for the probabilistic prediction of yield strength in electron-beam additively manufactured Ti-6Al-4V

by

Thomas K Ales

A thesis submitted to the graduate faculty

in partial fulfillment of the requirements for the degree of

MASTER OF SCIENCE

Major: Materials Science and Engineering

Program of Study Committee:
Peter Collins, Major Professor
Richard LeSar
Frank Peters

The student author, whose presentation of the scholarship herein was approved by the program of study committee, is solely responsible for the content of this thesis. The Graduate College will ensure this thesis is globally accessible and will not permit alterations after a degree is conferred.

Iowa State University

Ames, Iowa

2018

DEDICATION

For people who do stuff and make things, and the people who made things so I could do stuff. I present the stuff I did so hopefully you can make something.

TABLE OF CONTENTS

Page

LIST OF FIGURES v

LIST OF TABLES vii

ACKNOWLEDGMENTS viii

ABSTRACT ix

CHAPTER 1. INTRODUCTION 1

CHAPTER 2. BACKGROUND 5
Electron Beam Additive Manufacturing (EBAM) 5
The Thermal Problem 6
The Role of Aluminum in Ti-6Al-4V 7

CHAPTER 3. EXPERIMENTAL AND COMPUTATIONAL TECHNIQUES 10
Experimental Techniques 10
Metallographic Sample Preparation 10
Sample Preparation Workflow 12
Sample Characterization Techniques 13
Scanning Electron Microscopy (SEM): Morphology and Chemistry 13
Optical Microscopy: Morphology 15
Computational Techniques 16
Finite-Element Analysis (FEA) of the Thermal Problem 16

CHAPTER 4. THE ADDITIVE PROCESS MODEL 19
Model Inputs 19
The Goldak Heat Source 19
Modeling the Solid-to-Liquid Transition 23
Other Thermal Boundary Conditions 25
Making Use of the Hybrid Quiet Inactive Element Method 25
Geometric Configuration 28
Motion Control Model 30
Thinwall Build Considerations 30
Thickwall Build Considerations 31
Taylor Hardening 33

CHAPTER 5. THE LANGMUIR MODEL APPLIED TO ADDITIVE MANUFACTURING 34
Overview of the Langmuir Model 34
Implementation of the Langmuir Equation 35
Overview 35
Implementation within the ICME Model 36

CHAPTER 6. AN INTRODUCTION TO k-SRAS 39
Overview and Motivation 39
SRAS and its application to Ti-6Al-4V 40
Euler angle recovery – Proof of Concept 41
Preliminary Results of the Proof of Concept 45
Future Work 46

CHAPTER 7. PRELIMINARY RESULTS OF THE APPLICATION OF CHEMICAL AND PROCESS MODELS TO PROBABILISTICALLY PREDICT σ_{YS} IN TI-6AL-4V 48
Post-Processing Workflow 48
Experimental Dataset 48
Initial Simulated Dataset 49
Addition of the Monte Carlo Method 51
Thinwall Calibration Results 53
Thickwall Verification Results 55

CHAPTER 8. PRINCIPAL ACCOMPLISHMENTS AND FUTURE WORK 60
Principal Accomplishments 60
Future Work 60
A truly integrated model 60
Utilization of SRAS for Orientation Microscopy 64

REFERENCES 66

LIST OF FIGURES

Page

Figure 1.1: The materials tetrahedron. This materials science paradigm can also be expressed linearly as the processing-chemistry-microstructure-properties-performance paradigm. 1
Figure 1.2: Photo of a small EBAM component. The component weight is approximately 180 lbs. The substrate is 1" thick. 3
Figure 2.1: Patent schematic [8] from showing a typical EBAM head and chamber. 6
Figure 2.2: Fig 5a. from [5] showing a virtual experiment varying Al-content and its effect on σ_y. 8
Figure 2.3: Figure 17 from [2] showing the roles of the various strengthening mechanisms of Ti-6Al-4V and their percent contribution to overall yield strength. 8
Figure 3.1: BSE images of the three microstructures discussed in Table 3.1, in order of decreasing yield-strength left to right. 11
Figure 3.2: Specimen key for tensile samples. 12
Figure 3.3: Left: Backscatter image acquired at MARL showing typical β-Anneal morphology. Right: Thresholded version of the same image. White pixels are the β phase, black pixels are the α phase. 14
Figure 3.4: Simplified workflow of the finite-element process. 17
Figure 4.1: ABAQUS simulation showing the Goldak heat source distribution. The distortion of the zero-flux isosurface on the left side of the image when compared to the right side is due to inactive elements and not the heat source itself. 22
Figure 4.2: An illustrative thermal profile showing the effect of c_p^*. 24
Figure 4.3: Schematic showing how the UEPACTIVATIONVOL subroutine models deposition of material. 26
Figure 4.4: Nodal Temperature output for a thickwall simulation. The isosurfaces show the inactive elements forming a barrier to the beam directly ahead of the beam center, and on the far side of the layer. 27
Figure 4.5: Schematic representation of the thinwall build geometry. 28
Figure 4.6: Schematic representation of the thickwall build geometry 29
Figure 4.7: Plot showing the implementation of Eq. 4.9 30
Figure 6.1: CP-Ti (Left), Ti-6Al (Center) & Ti-7Al (Right) compliance surface plots. 41
Figure 6.2: Schematic showing an image of an a-lath normal and its relationship to the 0001. 43
Figure 6.3: Pyramid representation of the lath normal. 43
Figure 6.4: Overview of the registration method. a) Normal map computed from MIPAR pattern map. b) EBSD orientation map. c) Pre-registration overlay. d) Post-registration transformed overlay. 44

Figure 6.5: Comparision of the original Phi2 rotation in 60-degree space (L) with the SRAS-fused estimation of Phi2 (R)..... 46
Figure 6.6: SRAS Orientation map reconstructed from the ϕ_1, Φ and lath normal angle. An 8 degree rotation offset has been applied to minimize error..... 46
Figure 7.1: Flowchart describing how the various portions of the post-process model. 48
Figure 7.2: Probability Density Distributions (PDPs) for sample-000 assigned to the β-Anneal heat treatment. 52
Figure 7.3: Probability density fit for the thinwall after calibration. 54
Figure 7.4: Cumulative distribution plot for the thinwall dataset, post-calibration..... 54
Figure 7.5: Weibull probability plot for thinwall model, post-calibration. 55
Figure 7.6: Results for the AM-SR heat treat condition. Top-Left: Cumulative distribution. Top-Right: Probability density distribution. Center: Weibull probability plot. 57
Figure 7.7: Results for the HIP heat treat condition. Top-Left: Cumulative distribution. Top-Right: Probability density function. Center: Weibull probability plot. 58
Figure 7.8: Results for the AM-b-Anneal heat treat condition. Top-Left: Cumulative probability distribution. Top-Right: Probability density distribution. Center: Weibull probability plot..... 59
Figure 8.1: Ellingham Diagram for TiO_2 and Al_2O_3..... 61
Figure 8.2: Comparison of a small portion of billet oxidized in atmosphere (L), versus the oxide layer on an EBAM build..... 62
Figure 8.3:Raman spectra captured of a small portion of build. The sample is given in black, while the two standards used for comparison are given in red, and blue. 63

LIST OF TABLES

Page

Table 3.1: Applicable proposed nomenclatures for additively-manufactured Ti-6Al-4V from [10]. 10
Table 3.2: Summary of the imaging and EDS conditions. 15
Table 4.1: Typical Values used in all process models. 21
Table 4.2: Typical values used in simulations for modeling the solid-to-liquid transition, taken from [20]. 24
Table 4.3: Z-Offset flag and corresponding window dimensions. 32
Table 5.1: Values used in the Langmuir model for specific species. 38
Table 7.1: Inputs for the model taken from [2] unless noted. Deviation is given as the percentage of the value. 50
Table 7.2: Thinwall experimental dataset statistics, separated by heat treatment. 53
Table 7.3: Comparison of Average σ_{YS} between model and experimental results. 56

ACKNOWLEDGMENTS

I would like to thank Pete Collins, Richard LeSar, Frank Peters, Martin Thuo and Steven Kmiec. I would also like to thank Matthew Kenney for his work on helping with development of the ϕ_2 rotation recovery. Scott Wells also deserves special mention for his work on the physical database.

In addition, I would also like to thank the Iowa State High-Performance Computing Group, especially, John Dickerson, Jason Shuck and Cory Johns, and the Material Analysis and Research Laboratory (MARL), and Sensitive Instrument Facility at The Ames Laboratory along with Boeing, Sciaky Inc., Andrew Baker and Gary Harlow.

This research was funded in part under DARPA contract HR0011-12-C-0035, "An Open Manufacturing Environment for Titanium Fabrication," although the views, opinions and/or findings expressed are those of the author and should not be interpreted as official views or policies of the Department of Defense or the U.S. Government.

ABSTRACT

A complete model for the prediction of the yield strength of Titanium 6Al-4V in an additively manufactured component is presented herein. A thermal model is presented utilizing the ABAQUS simulation software to provide the process leg of the materials tetrahedron. The thermal model is fed into an implementation of the Langmuir equation that has been adapted for use in the simulation of the Electron-Beam Additive Manufacturing (EBAM) process. The predicted chemistry provided by the Langmuir equation for the Ti-6Al-4V alloy is then used in a phenomenological equation for the prediction of yield strength; a design probability curve is generated through random sampling of the thermal model. Using Weibull probability distributions, the model is verified against a rich mechanical and chemical database built from an actual EBAM build used in previous research.

CHAPTER 1. INTRODUCTION

Materials achieve their highest performance when the mutual influences of "structure, properties, performance and process," [1] are well understood not only in their individual, isolated contributions but also their interrelationships, shown in Figure 1.1.

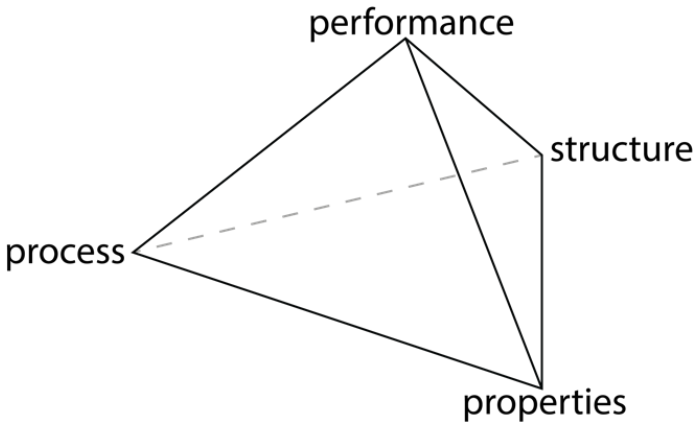

Figure 1.1: The materials tetrahedron. This materials science paradigm can also be expressed linearly as the processing-chemistry-microstructure-properties-performance paradigm.

Presently, these interactions are not well understood with regard to Additively Manufactured (AM) materials, although there have been efforts in individual areas, especially when compared to more traditional thermophysical processing routes which have matured over the span of decades. In previous work [2], a phenomenological model was developed for the prediction of yield strength (σ_y) in additively manufactured Ti-6Al-4V as a function of chemistry, and microstructure. By solving for the properties using the available chemical and microstructural information, the performance can be predicted. Performance, in the context of this thesis, is used in the same manner that a design engineer would use the term. That is, it is a statistically significant representation of samples that gives rise to 'design allowable' curves. Ideally, these design allowable

curves would either be predicted either completely or in part, reducing the number of required test specimens to develop an aerospace allowable curve from the 897 samples presently required.

Various AM processes exist, such as Selective Laser Sintering (SLS), Selective Laser Melting (SLM), Laser Engineered Net Shape (LENS) and Electron Beam Additive Manufacturing (EBAM). The first three methods are characterized by the use of a laser as the heat source, and can be performed either in an inert atmosphere, or vacuum environment. From literature, "Most laser-based systems have a maximum build rate of about 70 cm^3/h," [3]. In stark contrast, the EBAM process operates on a much larger scale with deposition rates up to 40 lb/h [4]. Assuming a material density of 0.00976 lb/cm^3 (converted from [5] for Ti-6Al-4V), this gives a volumetric build rate of approximately 4100 cm^3/h, several orders of magnitude greater than the more common laser-based processes. For the EBAM process, there is also the problem of operating under a vacuum compared to an inert atmosphere when using alloys that have elements with large differences in boiling point, such as Ti-6Al-4V. Figure 1.2 shows a small EBAM component, weighing approximately 180 pounds. However, builds in excess of 1000 pounds have been achieved using EBAM processes, with part build envelopes of up to "19 ft. x 4 ft. x 4 ft. (5.79m x 1.22m x 1.22m) or round parts up to 8 ft. (2.44m) in diameter," [6]

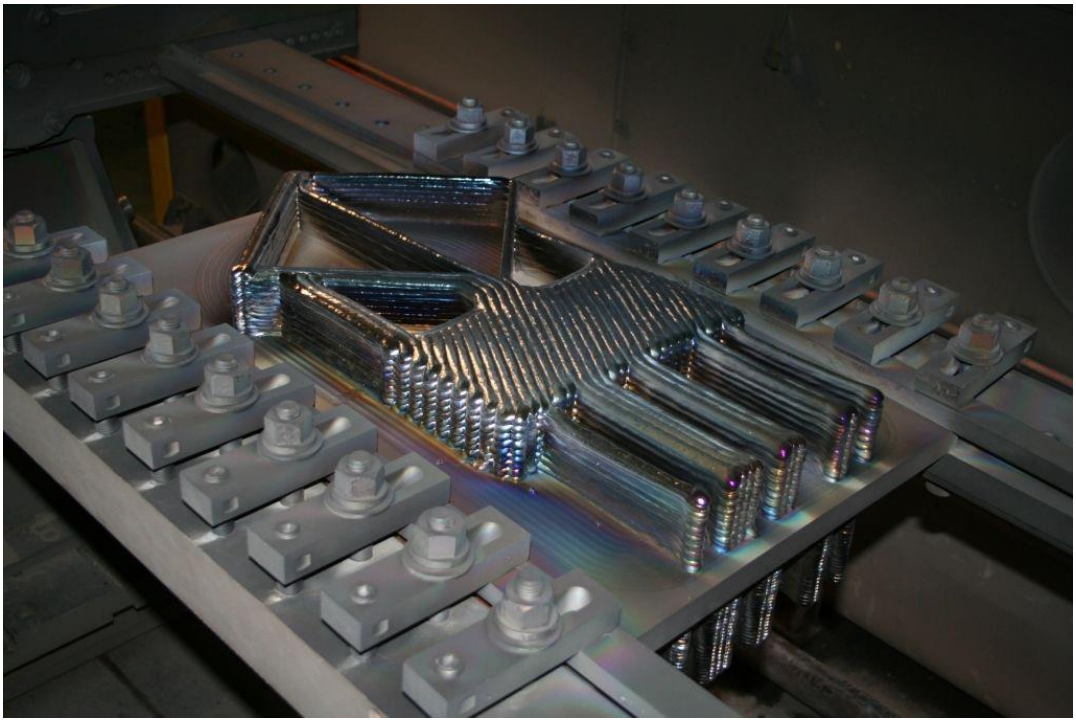

Figure 1.2: Photo of a small EBAM component. The component weight is approximately 180 lbs. The substrate is 1" thick.

A thermal process model is developed in this work for EBAM, providing the needed process linkage in the MSE paradigm, as it provides element-specific temperature-time histories, allowing the structure and chemistry properties to be predicted, followed by the resulting properties, and thus performance.

Although the particular framework presented is specifically for the commercial engineering alloy Ti-6Al-4V, it is based upon fundamental physics that are alloy agnostic and thus, there is no reason that it cannot be adapted for each alloy family or process of interest. Within this thesis, the models and attending theory are presented more as a specific example of an integrated approach and engineering philosophy, rather than a particular, optimized solution to the problem.

For calibration and verification of the model, a rich database consisting of more than 300 samples was developed and leveraged [2], along with Weibull statistical methods to allow the generation of a cumulative probability distribution function (CDF) and probability density functions (PDF). Weibull distributions are commonly used in the modeling of failure rates for components and form the basis of design allowable curves in many industries. These approaches permit multiple heat treatments for Ti-6Al-4V to be explored, and the results of 3 such heat treatments will be discussed later.

Further work will continue to push development of new techniques to help characterize and understand the effect of texture. To this end the integration of a device utilizing the principle of Spatially Resolved Acoustic Spectroscopy (SRAS) on to a Robomet.3D is discussed, which would enable much-needed large scale orientation microscopy. Some of the drawbacks of the method are shown, and preliminary results for a novel method of recovering the 3rd Euler angle are given. Recovery of the 3rd angle is performed through the fusion of a SRAS-like test dataset with an α-lath orientation map generated from a backscatter electron micrograph to mimic data that would be provided from an optical micrograph of an etched sample. These two datasets are then spatially registered against each other using a mutual information fitness function in the commercially available software package MATLAB.

CHAPTER 2. BACKGROUND

Electron Beam Additive Manufacturing (EBAM)

While there are detailed histories available for powder-based electron beam systems, like those developed by Arcam in the Wohler's Report [7], there is relatively little about wire-fed systems such as those supplied by Sciaky, Inc.

The first explicit mention of a wire-fed EBAM process to a US provisional patent #12883340, "Electron Beam Layer Manufacturing," [8] was filed by Scott Stecker, and assigned to Sciaky in 2011, this patent described the use of an electron beam source, and wire feed to manufacture a three-dimensional part via layers shown in Figure 2.1. A motion controlled stage moves in the X/Z direction, while the deposition head moves in the Y direction. Deposition can occur either in a single direction, or use both X/Z directions for deposition. The relatively large input wire diameters of approximately 0.125" limits the resolution of the components that the EBAM process can produce, but results in very high deposition rates, making the EBAM process suitable for very large parts. These EBAM preforms are near net shape and can then become equivalent input to a forging or billet for use traditional machining processes, but with the advantages of less waste and a higher fly-to-buy ratio in the finished component.

There are several significant differences in the EBAM approach, relative to the smaller scale processes of Selective Laser Melting (SLM) or Laser Engineered Net Shape (LENS). Two of these differences have a direct influence on the resulting metallurgy of the deposited material. First, there is the issue of energies, a typical LENS system may be powered by a 450-500W laser, whereas the EBAM beam power is set around 8kW for most Ti-6Al-4V builds.

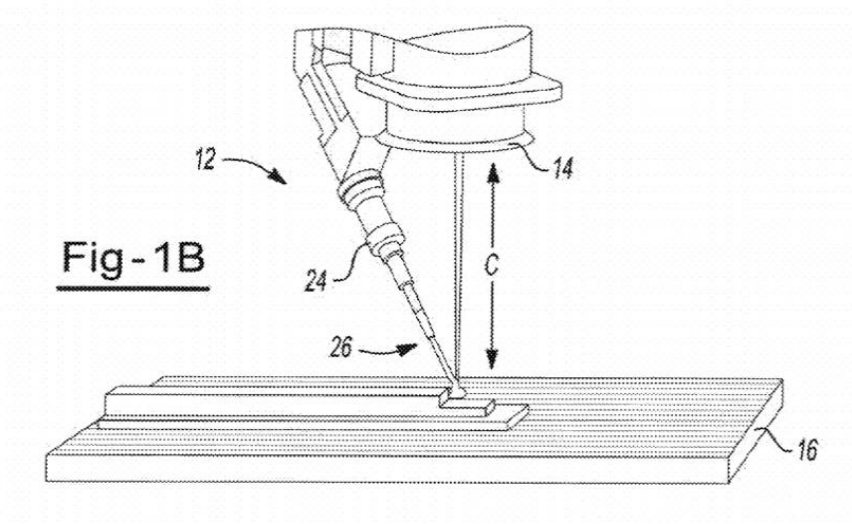

Figure 2.1: Patent schematic [8] from showing a typical EBAM head and chamber.

Secondly, is the issue of aluminum vaporization. Aluminum's boiling point is given as 2973K [9] at atmosphere. With thermal models showing the melt pool reaching temperatures in excess of 3600K, the loss of aluminum through vaporization is significant, and compounded by the free-expansion effect provided by the vacuum as compared to if the build was occurring in an inert atmosphere.

Currently the vaporization issue is dealt with by using input wire that is in excess of the target chemistry. Then relying on the vaporization process itself to bring the melt into acceptable limits for chemistry: usually between 5.5% - 6.5% by weight if one is trying to use ASTM B348 or F2924 equivalent chemistries in the final build. The current approach lacks rules to predict the chemistry differential and is typically Edisonian.

The Thermal Problem

In the literature, there are abundant solutions for solving the thermal problem [10-13]. A well-known collection of information regarding the thermal problem comes from the seminal work of Pan Michaleris, both with his group at Pan Computing (now part of Autodesk, Inc.), and the CIMP 3-D Center at Penn State, led by Richard Martukanitz.

Michaleris' work, "Thermomechanical Modeling of Additive Manufacturing Large Parts," [11], presents an efficient solution to the thermal and mechanical problem. The article presents several techniques including, but not limited to, "hybrid quiet inactive element activation," and "adaptive coarsening," of the element mesh to allow for solving of the thermal problem. Unfortunately, ABAQUS cannot feasibly implement the adaptive coarsening algorithm presented at this time, but it has incorporated some of the ideas in the "hybrid quiet inactive element" technique through the `UEPACTIVATIONVOL`[1] subroutine present in ABAQUS/2017 and later releases. This technique is discussed in further detail in Chapter 4, "The Additive Process Model." Although the simulations used in this particular implementation of the approach were done in ABAQUS, there is no reason that they could not be performed in a similar finite-element solver, provided the deposition of material and simulation of the radiative losses are handled.

The simulations presented in this work do not make use of the adaptive coarsening method, so they are not computationally efficient, and thus require the use of cluster computing, provided by the Iowa State University High-Performance Computing Group. The aim of this work though is to demonstrate the feasibility of integrating the multiple legs of Fleming's tetrahedron.

The Role of Aluminum in Ti-6Al-4V

Aluminum is the most widely used alpha stabilizer in titanium, including Ti-6Al-4V, and is capable of influencing the yield strength in excess of 70 MPa by only varying the aluminum content by 1 wt%, as shown in Figure 2.2 [5]. Owing to the formation of

[1] Anything appearing in a `monospaced` font refers to an actual software object, command, subroutine or function within a software package or programming language.

the α_2 (Ti_3Al) phase, the aluminum content is capped at 6.5 wt%, and details of acceptable chemistries is given in ASTM B348, one of the widely used standards.

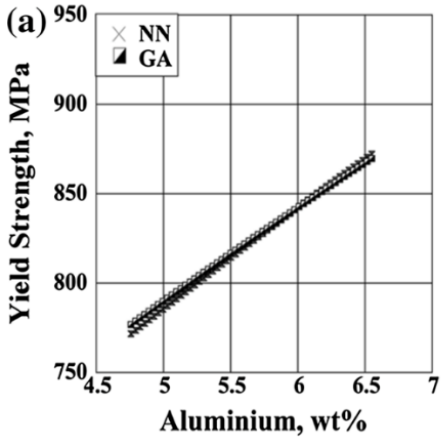

Figure 2.2: Fig 5a. from [5] showing a virtual experiment varying Al-content and its effect on σ_y.

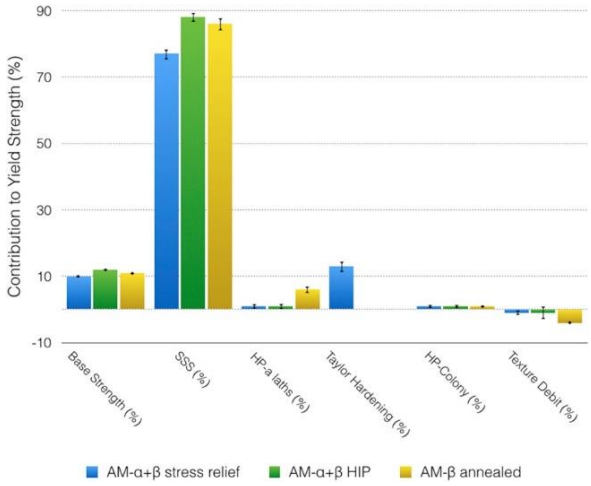

Figure 2.3: Figure 17 from [2] showing the roles of the various strengthening mechanisms of Ti-6Al-4V and their percent contribution to overall yield strength.

It must be kept in mind that the 70 MPa value claimed is given by a virtual experiment performed in previous work, and does not take aluminum's effect on the morphology of the alpha-laths, which may influence the yield strength through Hall-Petch effects due to the lath size. Virtual experiments permit the assessment of a single

variable (e.g., Al content) on the resulting material property. Such experiments would not be possible in real life due to the interrelated effects that chemistry has on structure and, by extension properties and performance. Figure 2.3, taken from [2] shows the various contributions and their relative contribution to the overall σ_{ys} of the material. High melt pool temperatures, vacuum conditions and the relatively large melt pool (12mm versus 50μm) compared to other additive processes, make the loss of aluminum a significant problem, when depositing Ti-6Al-4V with EBAM. Given that the yield strength changes significantly with the change in aluminum content this presents a problem for adoption of EBAM as a large scale process that can be used in high performance, low safety-margin applications.

Being able to intelligently predict, understand and compensate for possible solute loss during the EBAM build process is one of the key objectives highlighting the need for an integrated approach to understanding the material state in order to properly predict the properties and thus performance, and in so doing to provide designers and engineers with design allowables that exceed the minimum requirements imposed by a given application.

The provision of such predicted design allowables will notably accelerate the qualification of unique processing routes that additively manufactured parts present, but also presents a new paradigm for the qualification of other processes that include both additive and more traditional manufacturing processes and procedures.

CHAPTER 3. EXPERIMENTAL AND COMPUTATIONAL TECHNIQUES

Experimental Techniques

Metallographic Sample Preparation

The sample database used in this work was built initially for the research conducted on adapting a previously developed phenomenological model for wrought products for use with additively manufactured products [2]. As mentioned earlier, the database includes a large number of samples spanning three post-deposition heat-treatments. Using the proposed nomenclature from, "New nomenclatures for heat treatments of additively manufactured alloys," [10], these will be referred to as in Table 3.1:

Table 3.1: Applicable proposed nomenclatures for additively-manufactured Ti-6Al-4V from [10].

AM-Stress-Relieved	A fully lamellar microstructure. The features present in the as-deposited condition remain but may be coarsened. Spatial variation in the size and variants of α laths will remain.
AM-β annealed	A fully lamellar microstructure, typically consisting of elongated prior β grains with continuous grain boundary α, and with α-laths, existing as either colonies or basketweave. The spatial variation in the size and variants of α-laths will likely be eliminated (assuming constant composition and grain size).
AM-α+β Hot Isostatic Press (HIP)	Owing to the time and temperature details, these will be microstructurally similar to the AM-α+β high-temperature anneal. The important difference is that internal pores will be closed during the HIP cycle and the secondary alpha will be coarser due to slower cooling rate from HIP temperature.

These terms in Table 3.1 better reflect the actual processing that is encountered during a workflow involving an additively manufactured component compared to the typical labels, “as-received,” “mill anneal,” and “β-annealed” that are encountered in traditional thermomechanical processing routes. Representative micrographs along with their associated average σ_{ys} are given in Figure 3.1, note the scale of the center image is 20 microns as compared to the left and right image’s scale of 5 microns.

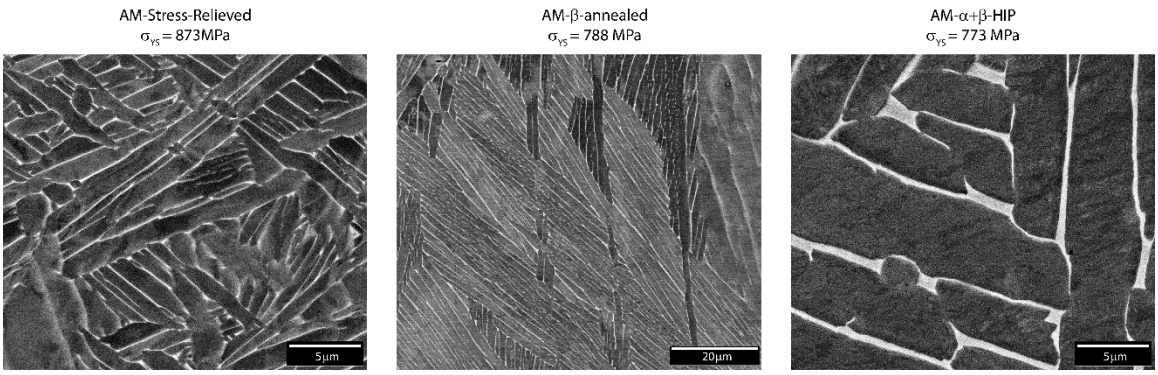

Figure 3.1: BSE images of the three microstructures discussed in Table 3.1, in order of decreasing yield-strength left to right.

The samples come from three different heat treatments, given below roughly in order of decreasing yield strength (σ_y). First is the AM-Stress-Relieved treatment condition, in which a part exposed to elevated temperatures, but well below any microstructurally active region in order to lower stress gradients induced by the build process. Notably, the dislocation density is still high for the AM-Stress-Relieved condition [2]. Second, is the AM-β annealed treatment, where the part is held at a high-temperature, allowing the growth of large α-colonies. Finally, AM-α+β HIP, in which the part is subjected to high-pressures and temperatures in the α+β phase field after the build in order to remove defects and stresses accumulated during build process. This high

temperature and pressure eliminates the high dislocation densities when compared to the AM-Stress-Relieved condition, with reported densities on the order of 10^{15} m^2 [2].

Sample Preparation Workflow

The samples contained within the database were prepared using standard metallographic practices. Samples were taken from precisely located positions of the build in the form of substandard ASTM round tensile blanks, described in ASTM E8/E8M [11], with a gage diameter of 0.250".

Following the tensile tests, which were performed by Westmoreland Mechanical Testing & Research (WMT&R), the longer half of the tested sample was selected for examination, and sectioned on a low-speed diamond saw, with a minimum thickness of 0.200" and at least 0.100" away from any visible necked region in order to minimize the influence of material plasticity on the microstructure. If this was not possible in the gage section, the sample was taken from the thread section and then the samples were mounted in conductive phenol (Buehler Konductomet) using a 1.25" diameter hot-press in groups of three, with unique geometric keys cut into each sample to identify it within the metallurgical puck, shown in Figure 3.2.

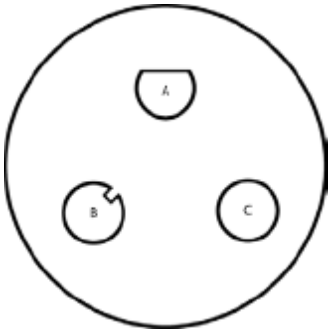

Figure 3.2: Specimen key for tensile samples.

Samples were then mechanically wet-ground in successively finer stages to 800 Grit / P2400 on Silicon Carbide (SiC) discs using a combination of hand-polishing and a Buhler EcoMet equipped with a power head. After grinding, the samples were polished to a mirror finish with a silica colloidal suspension (Allied Hi-Tech, 0.05μm, Rinsable/Non-Stick) cleaned ultrasonically in a mixture of soap (Allied Hi-Tech, GP Soap) and water, then ethanol followed by methanol. Following these washing procedures, the specimens were left in vacuum at 35°C to degas any solvent that may have infiltrated into the gap between the sample and phenol mount prior to examination. After examination using SEM, samples were etched using Kroll's reagent for 10-15 seconds, depending on sample reactivity and cleaned ultrasonically. The samples were optically examined.

Throughout the process each sample was traced back to the original location within the initial EBAM build via a database provided by the industrial sponsor of the research, which allowed for the generation of a spatially resolved dataset.

Sample Characterization Techniques

Scanning Electron Microscopy (SEM): Morphology and Chemistry

Each sample was examined in a FEI Quanta 250 FEG SEM using the Angular Backscatter Detector (ABS) in Z-Contrast mode. The instrument, located at the Materials Analysis and Research Laboratory at ISU, was also equipped with an Oxford Instruments Energy Dispersive Spectroscopy (EDS) system with a X-max 80mm^2 Silicon Drift Detector (SDD).

Between four and ten images were taken in backscatter mode with locations chosen at random, until the figures of merit described in, "Development of methods for the quantification of microstructural features in α + β-processed α/β titanium alloys," [12]

were met. These merit figures were set at a Coefficient of Variation (CoV) of $\overline{X_{VF\alpha}} \leq$ 3.0% for the α-phase volume fraction, and $\overline{X_{\alpha-lath}} \leq 10.0\%$ for the α-lath width variation and were then processed using the commercially available Materials Image Processing And Reconstruction (MIPAR) package [13].

To determine the volume fraction of the alpha phase, the properties of backscatter images were utilized. In Ti-6Al-4V, the α phase is darker than the β phase due to the difference in average *Z* within the two phases, as α stabilizers tend to be atomically lighter than β stabilizers [14] for Titanium, with tin being the notable exception to the rule. MIPAR is able to threshold and identify these regions in a batch manner once an appropriate recipe has been designed for the typical imaging condition.

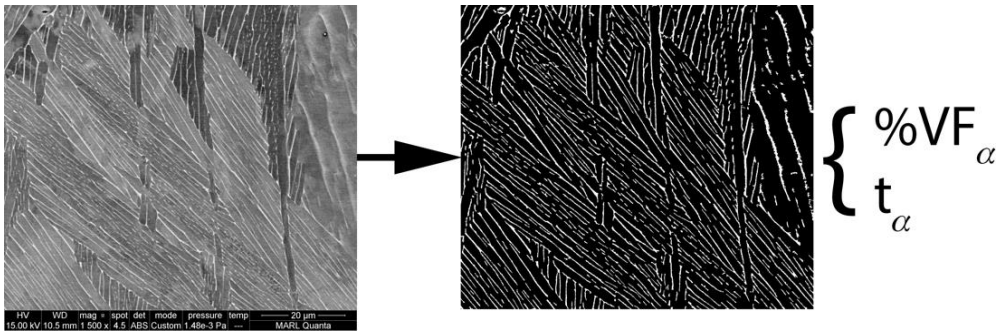

Figure 3.3: Left: Backscatter image acquired at MARL showing typical β-Anneal morphology. Right: Thresholded version of the same image. White pixels are the β phase, black pixels are the α phase.

EDS spectra were also acquired during the imaging of each sample. These spectra were deconvoluted against the default standards native to the Oxford AZtec software package. Each run was allowed to acquire 5M counts at the standard 'Process Time' setting of 4 with Pulse Pile-Up Correction enabled. This information was used in conjunction with chemical testing provided by Luvak Laboratories to provide location-specific chemistry for each sample.

Table 3.2: Summary of the imaging and EDS conditions.

Parameter	Setting
Accelerating Voltage	15kV
Spot Size (FEI)	4.0
Dwell	30 microseconds per pixel
Resolution	2048px FEI xT preset
Working Distance (EDS + BSE)	10.0mm
Final Aperture	30 microns
EDS Process Time	4

The BSE images then were processed in MIPAR. From these images, the volume fraction of the α-phase present, along with the α-lath thickness was extracted from each image and used to compile the statistical information for each sample.

Optical Microscopy: Morphology

Once the samples were satisfactorily examined and characterized in the electron microscope, they were etched in a bath of Kroll's Reagent for 10 to 15 seconds. This etching allowed for optical imaging of each sample. For the Prior-Beta Grain Factor (PBGF), one large overview mosaic was taken using an Olympus GX20 in brightfield mode at 5x magnification. Several more images were taken at 200x magnification to establish the percentage of α-Colony present, and the Colony Scale Factor (CSF) for the sample using stereographic techniques suitable for the task. The stereological analysis of optical images was completed in the commercially available software package, Adobe Photoshop CC, using a set of plugins known as Fovea Pro, the Fovea Pro plugins have

now been superseded by QIA-64, but provide similar functionality. QIA-64 is available from Reindeer Graphics, Inc.

Computational Techniques

Finite-Element Analysis (FEA) of the Thermal Problem

Due to the complex nature of the thermal history of an additively manufactured part compared its traditionally-processed counterpart, numerical simulation must be invoked. This is due to the unique and complex thermal nature of the build itself, the part-dependent thermal profile and the relatively complex geometries as compared to a traditional forging model, which may just involve a cylinder of a specified geometry, at an isothermal hold and a known, or desired reduction in area.

To get the part-dependent thermal solution, the ABAQUS FEA package is used, which is commercially available from D'assault Systemes. The ABAQUS package is known for its user-extensibility through FORTRAN and C subroutines and general-purpose design.

The finite-element method is can be summarized as follows: a geometry of interest is modelled, either internally to the finite element package or externally in another CAD program, such as CATIA, SolidWorks, or Inventor. This serves as the basis for the meshing software to create a discretized mesh to operate on. Boundary conditions are specified either through direct specification in the case of constant temperatures, fluxes, etc., or they are prescribed through the use of user subroutines, a simplified overview of this workflow is shown in Figure 3.4.

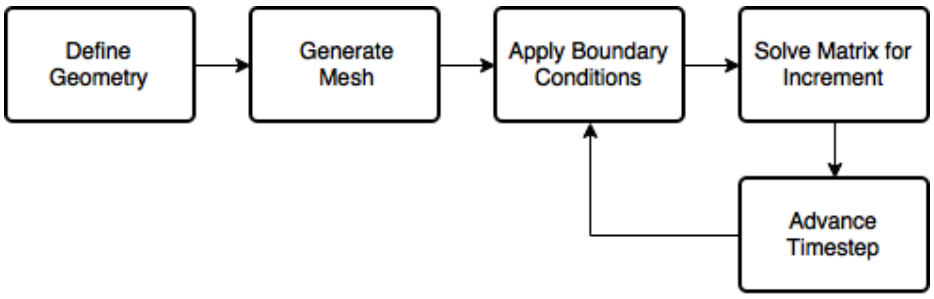

Figure 3.4: Simplified workflow of the finite-element process.

For the process model, the direct symmetric solver is invoked within ABAQUS, which uses Newton's method to handle the non-linear portion of the simulation, with a Gaussian elimination method for the linear portion to solve the basic energy balance equation given below in Equation 3.1 [15]. The left hand side of the equation represents the internal energy of the system, the density, ρ, is multiplied by the change in internal energy ($\dot{U}$) of the control volume (dV).

$$\int_V \rho \dot{U} dV = \int_S q dS + \int_V r dV \qquad \text{Eq. 3.1}$$

To handle the time integration in an uncoupled analysis, ABAQUS uses a backwards-difference algorithm, which allows the internal energy of the system to be described as the change in system energy between the two increments, and then scaled appropriately by the timestep the solver chose, as shown in Equation 3.2:

$$\dot{U}_{t+\Delta t} = (U_{t+\Delta t} - U_t)\left(\frac{1}{\Delta t}\right) \qquad \text{Eq. 3.2}$$

For uncoupled heat transfer, ABAQUS assumes that the system's internal energy is only controlled by temperature, but not any mechanical effects.

ABAQUS then can describe the internal system energy through specific heat, defined as the change in energy (dU) with respect to the change in temperature ($d\theta$):

$$c_p(\theta) = \frac{dU}{d\theta} \qquad \text{Eq. 3.3}$$

With the system defined, ABAQUS uses the Galerkin method to discretize the geometry that was specified during the setup of the problem. It then solves the system of equations until the appropriately specified error residual is reached or the maximum number of iterations has been reached for the increment. The time-step is determined by the user through the specification of the maximum allowable temperature increase in the increment. Currently, models are setup to capture frames at a maximum of every 100ms, while incrementing at approximately 1ms during deposition events. During cooling events the models report and increment at 500ms. In ABAQUS, this is controlled by specifying a 300K maximum increase per increment in the setup of the step. The reporting increments are controlled by specifying the reporting step in the “Time Points” portion of ABAQUS/CAE. The solver is then directed to use these model specific increments for reporting. This allows for non-uniform steps to save on the size of the resulting output databases. Only during the deposition events are the short timestep points required, as the cooling rates once below 1000℃ can be adequately modeled using a 500ms time increment.

CHAPTER 4. THE ADDITIVE PROCESS MODEL

Model Inputs

The Goldak Heat Source

The process model utilizes the Goldak double-ellipsoidal heat source [16] to model the electron beam as an asymmetric ellipsoid. The Goldak source was initially used for the modelling of electron beam welding and can capture an arbitrary distribution well. Other heat source models exist, such as the Rosenthal solution, but was not chosen due to the Rosenthal solution assuming the form of a point source [17]. Along with being able to customize the shape of each individual quadrant of the beam intensity distribution makes it a good choice for electron beam based processes that allow for fairly arbitrary (e.g., the beam does not need to be symmetric, or uniformly distributed) distributions. The model is implemented within the `DFLUX` subroutine of ABAQUS.

The computation of the heat source is a two-step process. First, a coordinate transform is performed to determine the position of the beam origin, as shown in equations 4.1 through 4.3:

$$x' = x_0 + v_x t \quad \text{Eq. 4.1}$$

$$y' = y_0 + f(step) \quad \text{Eq. 4.2}$$

$$z' = z_0 + v_z t \quad \text{Eq. 4.3}$$

Where *x'*, *y'*, and *z'* represent the current position of the beam in the global coordinate system as a function of the velocities v_x, and v_z, which are piece-wise polynomials that represent the motion of the beam. The layer height is controlled by the function *f(step)*, which must be coded for each specific geometry. Depending on how the steps within ABAQUS are logically organized and linked to the actual change in layer

determines the approach one must take when developing the *f(step)* equation. Second, the flux field is calculated based on the beam origin. The power densities are given by Equation 16 in [16] and is adapted for use in the model as Equation 4.4 below. The power distribution function requires the determination of three characteristic length values: *a, b,* and *c,* which correspond to the *x, y* and *z* axes of the heat source ellipsoid. The layer geometry measured approximately 0.50" in width, and 0.25" in thickness, so these values were used directly, and are shown in Table 3.2.

Information regarding the suitable front and rear hemisphere characteristic values was not available, so the advice provided by Goldak, et. al., was followed:

> "In the absence of better data, the experience of these authors suggests it is reasonable to take the distance in front of the heat source equal to one-half the weld width and the distance behind the heat source equal to twice the weld width" [16].

Regarding the front to rear power split, Goldak's approach was similarly taken:

> "Values of $f_f = 0.6$ and $f_r = 1.4$ were found to provide the best correspondence between the measured and calculated thermal history results."

Shown below in Eq. 4.4 is the heat flux *(q)* as a function of the global beam origin position. *Q* represents the magnitude of the beam, and *f* is the distribution fraction, which should sum to 2.

$$q(x', y', z') = \frac{6\sqrt{3}fQ}{abc\pi\sqrt{\pi}} \exp\left[-\frac{3x'^2}{a^2}\right] \exp\left[-\frac{3y'^2}{b^2}\right] \exp\left[-\frac{3z'^2}{c^2}\right] \qquad \text{Eq. 4.4}$$

Table 4.1: Typical Values used in all process models.

Symbol	Measured Value	Calculated Value
Q	8200 W	-
a / r_{beam}	0.250 in	-
b	0.125 in	-
c_{front} / c_{rear}	-	0.250” / 1.000”
v_{avg}	30 inches / minute	-

Figure 4.1 shows a visualization of the heat source in W/m^3. The ABAQUS state variable HFL (“Heat FLux”) is used to visualize the flux field. The blue isosurface represents a 0 W/m^3 flux. On the left-hand side of the image, there is a slight distortion of the zero flux isosurface due to the quiet element method that is discussed later. This distortion is to be expected with using a coarse mesh, such as the one in Figure 4.1.

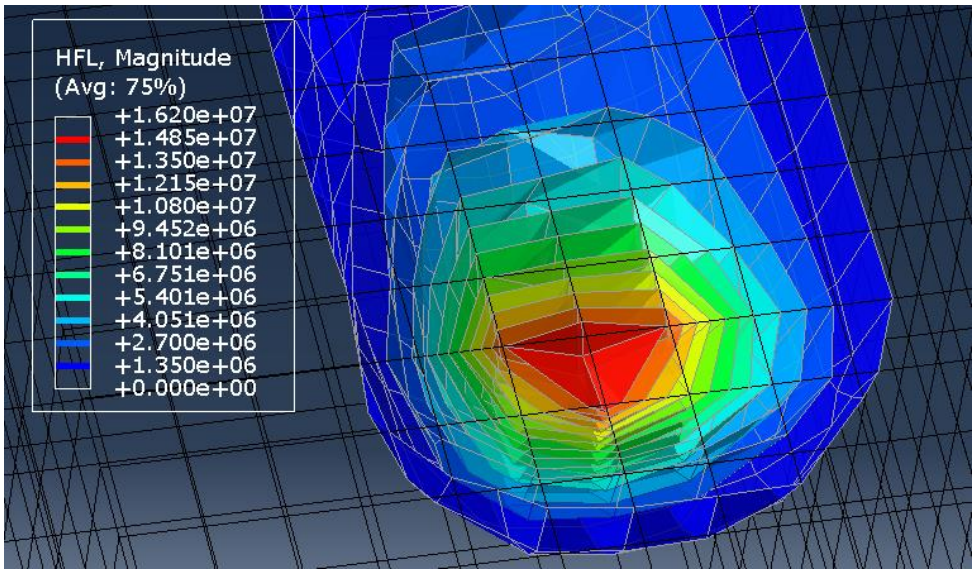

Figure 4.1: ABAQUS simulation showing the Goldak heat source distribution. The distortion of the zero-flux isosurface on the left side of the image when compared to the right side is due to inactive elements and not the heat source itself.

As shown in Figure 4.1, some of the known issues of using the "quiet element" method described in [18] are visible. Because ABAQUS and other FEA packages interpolate between node points any element that is inactive but immediately adjacent to another element will have a temperature error and also a heat flux error due to the sudden scaling of the specific heat and thermal conductivity. Meshing should be done with care in order to minimize the error zone, but also can be minimized through careful selection of k_s and $c_{p,s}$ as described in [18].

The input power (Q) was determined via build telemetry supplied by Sciaky, Inc. and was calculated as the average product of the measured input voltage on the beam and measured current in the workpiece, an average velocity of 30 inches per minute was also observed in the data, however, acceleration and deceleration of the head was not taken into account. Physical dimensions of the layers were measured on a thinwall specimen. Small adjustments were made to the flux distribution functions until the expected peak

melt pool temperatures were observed. Using the above guidance provided by Goldak, there was approximately a -400K differential between the simulated and expected peak melt pool temperatures. The distribution was successively shrank, so that the peak temperature would increase, it was found that setting a / r_{beam} equal to 0.200" gave good agreement with the expected peak pool temperature.

The heat source is realized through the ABAQUS user subroutine `DFLUX`. `DFLUX` allows for specification of arbitrary, point, surface and volume fluxes within a simulation domain.

Modeling the Solid-to-Liquid Transition

If the value of the latent heat of fusion is known, and the freezing range of the alloy is also known, the calculation of the effective specific heat is a trivial exercise and computationally efficient [19], shown in Eq. 8. For Ti-6Al-4V, values of 330 kJ/kg for Δh_f and 10K for ΔT_f were used from [20]. This leads to an effective heat capacity of approximately 33 kJ/kgK for the solidification event. With this information the full thermal profile can be simulated, as shown in Figure 9. As the point cools from the peak melt temperature, only sensible heat is lost, as the upper end of the freezing range is reached, the effective heat capacity is used to account for the correct amount of latent heat required to solidify the material.

$$c_p^* = \frac{dU}{d\theta} = \frac{\Delta H_f}{\Delta T_f} = 33\,\frac{kJ}{kgK} \qquad \text{Eq. 4.5}$$

Table 4.2: Typical values used in simulations for modeling the solid-to-liquid transition, taken from [20].

Symbol	Typical Value
T_{melt}	1933K
ΔT_f	10K
Δh_f	330 kJ/kg
$c_{p,s}$: $T < T_{melt}$ c_p^* : $T_{melt} < T < T_{melt} + \Delta T_f$ $c_{p,l}$: $T_{melt} + \Delta T_f < T$	$c_{p,s}(T) = (8 \cdot 10^{-5})T + 0.7019$ $c_p^* = 33.0\ kJ/kgK$ $c_{p,l}(T) = (-6 \cdot 10^{-6})T + 1.1441$

Once through the solidification event, the solid heat capacity equation takes over and resumes modeling the heat capacity. This approach can also be used to account for any exothermic or endothermic effects from phase changes in other alloys or material systems.

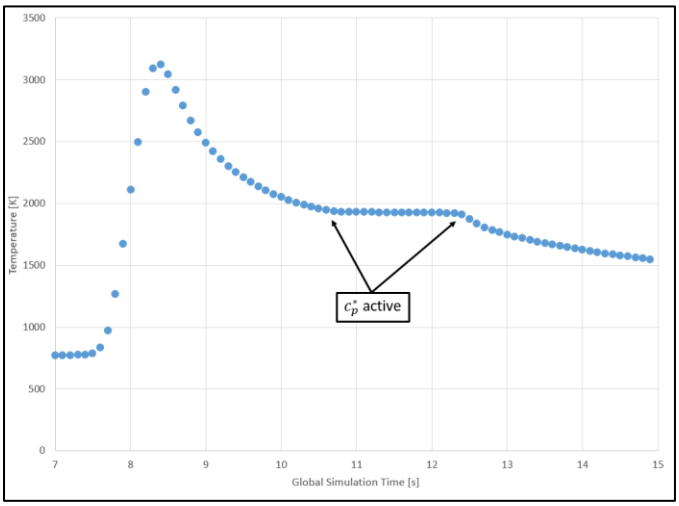

Figure 4.2: An illustrative thermal profile showing the effect of c_p^*.

Other Thermal Boundary Conditions

The other significant contributor to the character of the thermal profile seen in the EBAM process is the loss of heat energy via radiation. In ABAQUS, this is modelled using the Stefan-Boltzmann relationship for radiation loss, shown in Eq. 4.6. The primary value that controls the loss rate is the emissivity (ε), set here to a constant value of 0.77 for titanium. ABAQUS abstracts the contribution from the Stefan-Boltzmann constant and the emissivity value ($\sigma = 5.67 \cdot 10^{-8}\ W/m^2K^4$) into a single constant (A) [21]. θ is the surface temperature, and θ^o is the infinite sink temperature.

$$A = \sigma\epsilon;\ \ q_r = A\left(\theta^4 - \theta^{o4}\right);\ \ \frac{\delta q}{\delta \theta} = 4A\theta^3 \qquad \text{Eq. 4.6}$$

Making Use of the Hybrid Quiet Inactive Element Method

The "hybrid quiet inactive element," method proposed and outlined by [22] is now part of the ABAQUS/2017 core functionality and is handled by the user subroutine `UEPACTIVATIONVOL`. It is worth going over however at a high level, as the process may not be intuitively obvious at first.

The ABAQUS software package does not allow for the `*MODEL CHANGE` keyword to be used in steps that have the `*PROGRESSIVE ELEMENT ACTIVATION` keyword active in the same step. This method then by Michaleris in [18] which used inactive elements to speed computational time on initial layers, and quiet elements to efficiently model the deposition of material, this approach only involves the quiet elements, and not any inactive elements. Inactive elements would be removed from the model and significantly speed computational time up. The quiet elements are present but characterized by having significantly lower c_p and k values as compared to a normal finite-element.

$$c_{p,quiet} = s_{c_p} c_p \quad \text{Eq. 4.7}$$

$$k_{quiet} = s_k k \quad \text{Eq. 4.8}$$

According to [18] , scaling factors of approximately $s_k = 1 \cdot 10^{-4}$ for the quiet element's thermal conductivity and $s_{cp} = 1 \cdot 10^{-2}$ for the specific heat scaling provided the best balance between activation error and stability of the Jacobian contribution for s_{cp} and s_k respectively, contributing an error of less than 0.25% compared to if the elements were left in the activated state.

The simulation determines which elements to activate by first determining the position of the beam within the current layer, and proceeds to activate all elements that are within the build domain, but behind the current beam position along the build path, schematically illustrated in Figure 4.3, the green elements are active, while the gray elements have been quieted. Once this is complete, a search for any build elements that are below the current layer plane is performed, and all found elements are activated before running the simulation for that increment. Figure 4.4 shows a NT11 (Nodal Temperature) distribution for a thickwall simulation, and shows how the quiet elements prevent any heat transfer into the inactive layer.

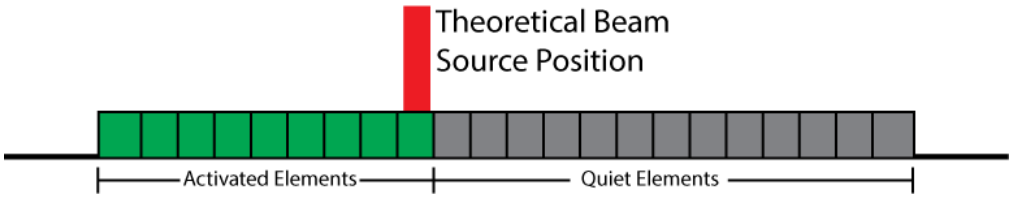

Figure 4.3: Schematic showing how the UEPACTIVATIONVOL subroutine models deposition of material.

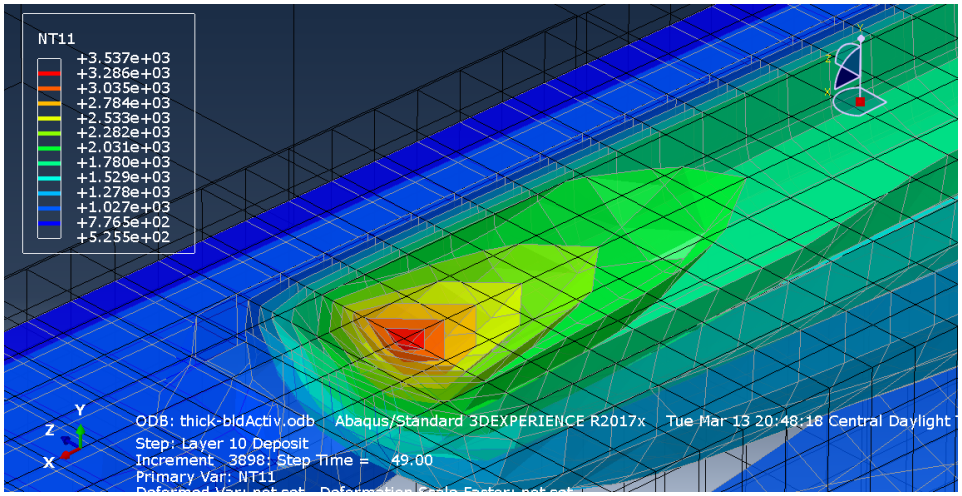

Figure 4.4: Nodal Temperature output for a thickwall simulation. The isosurfaces show the inactive elements forming a barrier to the beam directly ahead of the beam center, and on the far side of the layer.

Once an element is activated, it is no longer considered by the `UEPACTIVATIONVOL` subroutine if the element ends up in another search. In ABAQUS, each deposition step and cooling step for the layer is segmented into its own "Step" in the simulation. This provides a logical break using the `TIME(2)` component of the TIME array. In ABAQUS, `TIME(1)` is the global simulation time, and `TIME(2)` is the step simulation time. By allowing each layer to have its own deposition and cooling step, one can infer which step the simulation is on by doing a simple modulo division operation on the step number indicator, `KSTEP`. If `KSTEP` is odd, a deposition event is occurring, and the current layer should be activated in a progressive manner. If `KSTEP` is even, an interlayer cooling event is occurring, and the current layer should be fully activated so it can simulate the cooling that would occur in the actual build process as the deposition head returns to the home position.

Geometric Configuration

Two configurations are presented in this work that are relevant to the EBAM process. The thinwall geometry, which consists of a 12” x 12” x 1” plate acting as the substrate. Ten layers with a geometry of 10” x 0.50” x 0.25” are deposited to the center of the plate as shown in Figure 4.5. This geometry was chosen due to thinwall structures having a significant presence in additively manufactured components. The thinwall should also exhibit the highest cooling rates that the process should see as the substrate acts like a large thermal reservoir causing the first layer to cool significantly quicker than others. The small thermal mass of the single-pass thinwall structure compared to the volume of the heatsink amplifies this effect.

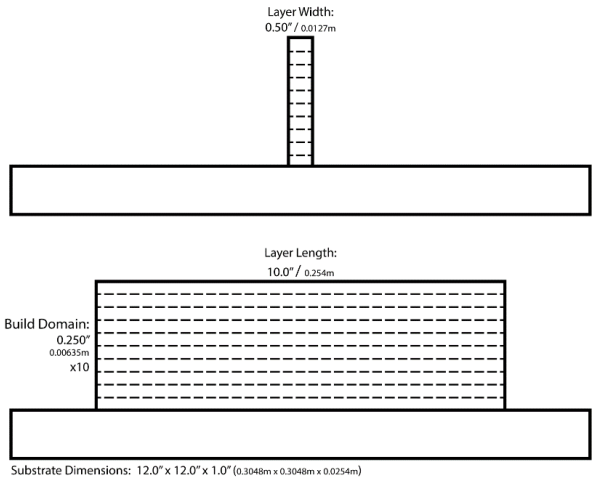

Figure 4.5: Schematic representation of the thinwall build geometry.

The second geometry presented is what is referred to as a thickwall build section and consists of three layers deposited side by side. This geometry stalls the cooling rates through the microstructurally active regions for longer compared to the thinwall geometry. A schematic representation of the thickwall build domain is shown in Figure

4.6 with the individual layers traced out by the dashed lines. The activation order of each layer proceeds from left to right in the schematic side view.

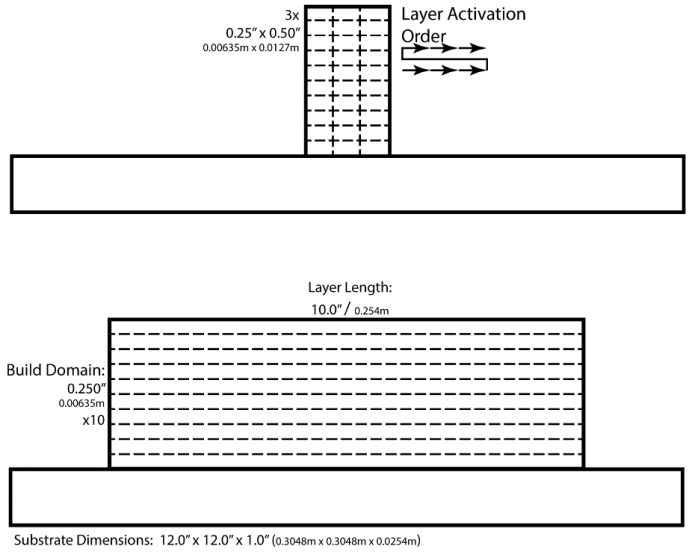

Figure 4.6: Schematic representation of the thickwall build geometry

Between each layer, an interlayer cooling time is provided to mimic the return of the head to the home position before deposition of the next layer. In these simulations, the interlayer cooling time has been set equal to that of the layer deposition time. For example, if a deposition takes 20 seconds, the total layer time, with the interlayer cooling time is 40 seconds.

From telemetry supplied by Sciaky, Inc. an average deposition speed of 30 inches per minute has been determined. For the 10" long builds that are modelled in this simulation, this leads to global simulation times of 420 seconds for a thinwall build, and 1,260 seconds for the thickwall build.

Motion Control Model

The motion controls were coded on a per case basis, but take the same overall modelling approach. In each case, the ABAQUS concept of a "Step" is used to control the current layer deposition. Repetitive motion is then modelled using modulo division in order to allow for arbitrary and infinite periodicity.

Thinwall Build Considerations

The thinwall configuration breaks deposition and cooling pass into their own ABAQUS "Step," as previously described an odd/even test is performed to determine if the step is a deposition or cooling step. The layer position is controlled by a function that takes the current simulation step and calculates the nearest integer layer. This function is given below in Eq. 4.9, `NINT()` is a FORTRAN function that returns the nearest integer. `KSTEP` is the ABAQUS environment variable that indicates the current layer step. This behavior is shown in Figure 4.7.

$$LayerNo = NINT(0.5 * REAL(KSTEP) + 0.5) \qquad \text{Eq. 4.9}$$

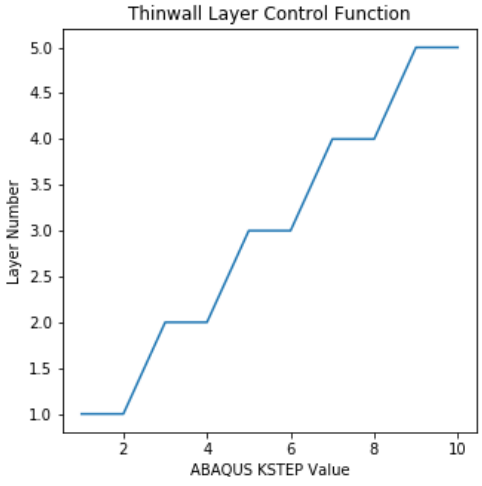

Figure 4.7: Plot showing the implementation of Eq. 4.9

Because each deposition and cooling stage is broken into its own step, and the only direction of motion is in the global x-direction, the step time, `TIME(2)` is used to provide the periodicity required by the motion equations. At the end of each step, `TIME(2)` returns to zero, and the beam position is returned to the home position.

Thickwall Build Considerations

The thickwall build has some unique challenges associated with it that require a different approach to how each layer is broken up into steps compared to the thinwall. Taking the same approach as the thinwall geometry would create 60 steps, which then each require their own logic code, boundary conditions, interactions and other specifications to be provided. In order to keep the number of steps required for these proof-of-concept models low, an approach that exploits modulo division is taken. A thickwall layer is 1.5” wide, it can be thought of as three 0.5” thinwall layers placed side by side. Time-wise is also the same as depositing three thinwall layers, which would take 126 seconds if we assume the same interlayer cooling time as the thinwall. By setting each step in ABAQUS to represent the deposition of an entire thickwall layer means the motion must be described in two dimensions. The first motion parameter that is determined is the z parameter. By dividing the current step time `TIME(2)` by the time it takes a thinwall layer to deposit (in this case 42 seconds) and then flooring that value to the nearest integer allows for simple case logic or if logic in the `UEPACTIVATIONVOL` subroutine. The values are provided in Table 4.3.

Table 4.3: Z-Offset flag and corresponding window dimensions.

Z-offset flag	Lower *Z* bound	Upper *Z* bound
0	-0.75”	-0.25”
1	-0.25”	0.25”
2	0.25”	0.75”

The next consideration is moving the beam along the x-axis, knowing from the thinwall build that it takes about 21 seconds to traverse the layer, and another 21 seconds to cool. By dividing TIME(2) by modulo 42, the cooling and deposition steps can be handled in one line of code. The first 21 seconds deposit as normal, the next 21 seconds, the beam is outside of the layer domain boundary and is ignored. Although this is not the most efficient method, it is very simple to implement and ABAQUS’ temperature driven time-stepping algorithm allows for simulating both the deposition step at 1ms, then the cooling steps at 500ms. The computational penalty is acceptable for demonstration purposes, one would want to more efficiently model the cooling steps, and allow ABAQUS to skip calculating the volume flux load.

Presently motion controls must be developed on a case by case basis for each geometry one wishes to investigate when using this method. While this is acceptable for research purposes, where the cases are idealized, it is worth the investment of time and effort to develop a g-code translator that would allow limited investigation of potential hot-spots and ‘bad’ geometric configurations on a case-by-case basis. This could be achieved either through the Python or C APIs that ship with ABAQUS.

Taylor Hardening

Taylor hardening was recently added to the phenomenological equation by Collins [2] and was a refinement of what was a somewhat arbitrary basketweave factor [5]. Taylor hardening is given by Eq. 4.10 and is shown below. Presently, it is not well understood when Taylor hardening is present in the model, but is activated for the stress-relieved components in the build. a is the prefactor term (set to 1 here), *M* is the Taylor Factor (set to 3.2 here), *G* is the shear modulus of the material, *b* is the Burger's vector and ρ is the dislocation density.

$$\sigma_{TH} = \alpha M G b \sqrt{\rho} \qquad \text{Eq. 4.10}$$

In previous work by Collins [5], this hardening was accounted for by the inclusion of a 'basketweave factor'. In the refinement done by Hayes [2], it was found that the Taylor hardening mechanism is active when the b-rib thickness is below a critical value. That value is presently unknown, however the experimental dataset for the AM-Stress-Relieved samples exhibited approximately a 30ksi deficit, when modelled using typical values for Ti-6Al-4V, previous research [2] has shown that a likely explanation for the discrepancy is Taylor hardening due to higher than normal dislocation densities present, on the order of 10^{15} m^{-3}.

CHAPTER 5. THE LANGMUIR MODEL APPLIED TO ADDITIVE MANUFACTURING

Overview of the Langmuir Model

Irving Langmuir's model for the vaporization of metallic tungsten [23] has been co-opted and adapted for use of modelling the vaporization of aluminum and uptake of oxygen during the AM build process. Langmuir's primary application of his model for to determine the evaporation rate of tungsten filaments during his work for General Electric. In vacuum, his model can be expressed using Eq. 5.1, shown below.

$$\dot{m} = \sqrt{\frac{M}{2\pi RT}} \cdot p(T) \qquad \text{Eq. 5.1}$$

In this context, *M* is the molar mass of the species of interest, *R* is the universal gas constant, *T* is temperature, and *p(T)* is the vapor pressure of the species of interest as a function of temperature. Semiatin & Kobryn showed that the Langmuir equation could be adapted for use in the modelling of vaporization Aluminum for casting of Ti-6Al-4V [24]. Collins, et. al. applied the model to additive manufacturing in [25] showing how the equation could be used to model both the vaporization rate of aluminum and the absorption rate of oxygen in a "leaky" inert-gas AM system with poor atmospheric controls.

This model is implemented in Python 3 and operates on thermal histories supplied by ABAQUS, using a simple numerical summation method to account for and model the loss of rates of various species of interest.

Implementation of the Langmuir Equation

Overview

The loss modelling is done as a separate script, once thermal histories have been identified and exported as a comma-separated value (CSV) file. The Langmuir equation assumes there is a boundary that is boiling vapor. A small control volume is assumed, in this case, 0.1 x 0.1 x 0.1m, and an emission surface area is assigned. Comparison with several samples determined that an emission area of 0.08 x 0.08m was acceptable and provided good agreement with samples that were used for the calibration step. The element size may seem large, but the surface to volume ratio appears to be the controlling factor rather than element size. Although the surface area to volume ratio was only calibrated against the aluminum, it was assumed that the same ratio should apply for the oxygen uptake in the build.

The CSV file is exported in the format shown below, a script to automate the export process has been written to work within the Python 2.7 interpreter that ships with ABAQUS:

```
#Path,someAutoGeneratedPath-001
#Sample Location:,0.000m,0.000m,0.000m
#Output DB:,someDatabase-final.odb
TIME,NT11,Z_COORDINATE,NT11,Z_COORDINATE
0.000,773.15,0.000,773.15,0.000
```

The # at the beginning of the line signifies that the line is header information and is not to be imported. Each file is then imported into a pandas `DataFrame`, allowing all thermal histories to be indexed along the same timeline. The odd configuration of the CSV is due to the output being adapted from an earlier script that was designed to export

multipoint paths over a time-series. The extraction script, much like the author's cat, is incapable of understanding the concept of a point, and it is simply defined as a path with the same start and end point, hence the duplication of the data. If one was concerned about execution efficiency they would make use of the C bindings that ship with ABAQUS, instead of relying on the Python bindings, which are significantly slower, but also easier to implement than the equivalent C routine.

Once all thermal histories have been assembled into the `DataFrame`, the time step is calculated using a backwards difference, with a simple piece of code to handle the first-entry edge case, where the script assumes the time step is the reported time. The vapor pressure is then calculated according to the reported temperature if required, and the loss-rate for the reported temperature is calculated. This is then scaled according to the surface area of emission and the time step. In this context, $\dot{m}$ is the output of Equation 5.3 for the species of interest. If modeling the vaporization of material, the sum should be subtracted from the initial mass, if modeling absorption, the sum should be added. To find the initial masses of the control volume, the density (ρ) is multiplied by the control volume (V) and multiplied by the mass fraction (X) of the species in the alloy.

$$m_{initial} = \rho V X \qquad \text{Eq. 5.2}$$

$$m_{final} = m_{initial} \pm \sum_{i=t_0}^{t_f} \dot{m}(t_i - t_{i-1}) \qquad \text{Eq. 5.3}$$

Implementation within the ICME Model

Aluminum is modelled as a loss, using the vapor pressure equation provided by Alcock, et. al. in [26] and is given by Eq 5.4 below:

$$p_{Al}(T) = 10.917 - 16211/\mathrm{T} \qquad \text{Eq. 5.4}$$

Where T is the temperature in Kelvin, and p_{Al} is the partial pressure of aluminum in Bayres. A Bayre is equal to one tenth of a Pascal. Langmuir's formula was originally developed for the centimeter-gram-second system and has been left unadapted to mks.

Oxygen is modelled similarly, except instead of using the vapor pressure to determine the mass flow rate, the ambient chamber pressure was used. It was then assumed that this was a standard atmospheric composition of 20% O_2. This provided the partial pressure for the oxygen uptake into the material.

There is however a sensitivity due to the modelling technique used. Currently each point is assumed to have a finite element and is modelled independently. The loss-accounting occurs within this element and not within any particular ABAQUS element. Therefore, the ratio of the emitter surface area to the volume of the model element has to be calibrated presently against existing data. Further work would include this as an ABAQUS user element subroutine, which would allow for the assignment of a boundary condition to better reflect the actual influence of geometry on the final chemistry of the build. This would be much more work than is implied, due to the need to create a unified "thermal-Langmuir" type element, that both performed the heat transfer functions, and the solute loss and absorption accounting. Otherwise, one would need to resort to a co-simulation or other technique to capture the data more accurately.

Table 5.1: Values used in the Langmuir model for specific species.

Parameter	Value	Source / Justification
M_{Al}	26.981 g/mol	NIST – SP 966 [27]
M_{O2}	31.998 g/mol	NIST – SP 966 [27]
R	8.3145 J/molK	NIST – SP 966 [27]

It should be evident that the Langmuir model is not a complicated one, but provides sufficiently accurate results. This simplicity is the model's greatest strength in design, as it does not require much computational horsepower, nor does it require a synthetic thermal profile. One could imagine using this in-line with a thermal camera / pyrometer or through appropriate spectroscopic methods to determine what the aluminum / oxygen content should be within the build and then verify, potentially allowing an operator to stop the build if it was to fall irrecoverably out of a chemical or mechanical specification.

Another scenario would be during the deposition of the first layer, the volume of the substrate compared to the volume of the layer is much greater and acts as a thermal reservoir. Currently, high aluminum content wire is used in builds to meet ASTM B348 or an equivalent. If the melt-pool temperatures of the first few layers are too cold, it is possible those layers can be out of chemical specification. One could imagine being able to identify this in real time and issue extra pass commands where the material is brought just above the melt point to vaporize off extra aluminum and fall back into specification.

CHAPTER 6. AN INTRODUCTION TO k-SRAS

Overview and Motivation

Although the model is capable of predicting the yield strength of AM Ti-6Al-4V in a satisfactory manner, the problem of texture remains. Ti-6Al-4V is predominantly the hcp α-phase. Being hexagonal, with a c/a ratio of approximately 1.33 leads to significant anisotropy depending on orientation relative to load.

The role of texture in Ti-6Al-4V, especially in the context of additive manufacturing has been examined in previous work by Collins [25]. Previously the only method known to the research group for the investigation of texture was Electron Backscattered Diffraction (EBSD) at this length scale or above in the US.

EBSD is known for being unforgiving when it comes to sample preparation. The interaction volume is approximately on the order of 100nm, and so any surface deviation or imperfection greater than that will cause a loss of signal. In addition, the operator is limited to the acceptable geometry allowed within the Scanning Electron Microscope, keeping in mind that the published microscope space envelope will be severely reduced due to the stage being tilted to 70 degrees for a good front-scattering EBSD detector take-off angle.

Spatially Resolved Acoustic Spectroscopy (SRAS) is an ultrasonic technique that effectively allows for visualization of the compliance surface. An early description of the SRAS system is given in [28] by M Clark and SD Sharples. There are many variants of SRAS that can have different applications. The most interesting variant to the author is the implementation known as k-SRAS, which according to work by Li can be described as,

> "A SAW velocity model is developed according to the elastic constants and mass density of the material. The orientation of crystals can be determined by comparing the SRAS results and the SAW velocity model" [29].

SRAS has the capability to recreate the data that would typically only be obtained via EBSD or Precession Electron Diffraction (PED), but at scales in excess of 10,000 times in area compared to EBSD [30] and approximately 10^9 larger in area than PED. In this section, several of the advantages and disadvantages are talked about with regards to SRAS and Orientation Microscopy (OM), present efforts to integrate SRAS into a piece of equipment to enable the development of what was termed a, "sonic twin," by the inventor of the technique [30], while simultaneously developing a 3-dimensional microstructural twin.

SRAS and its application to Ti-6Al-4V

Previous research has shown SRAS to be excellent in speed and area of acquisition in Titanium based systems [31]. However, the compliance surface of titanium is symmetric about the c-axis or 0001 direction in hcp α-phase as shown in Figure 6.1 below. Although there is an ambiguity problem in Figure 6.1, the direct change in compliance surface between CP-Ti and Ti-7Al could lead to the inference of chemistry in EBAM manufactured materials.

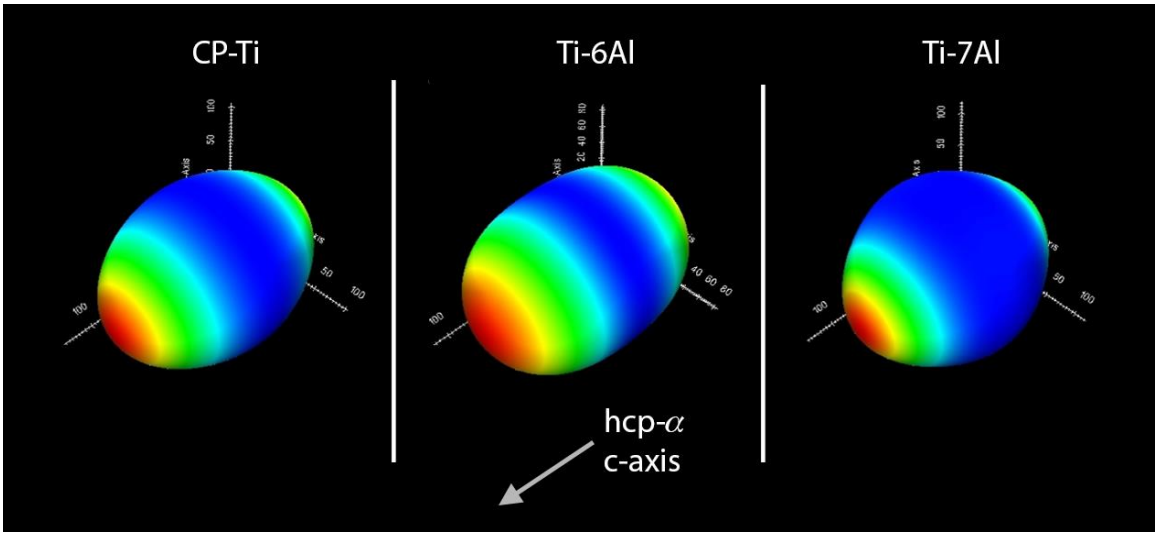

Figure 6.1: CP-Ti (Left), Ti-6Al (Center) & Ti-7Al (Right) compliance surface plots.

The database developed shows that titanium and vanadium fractions, along with interstitial chemistry stays relatively stable.

This directly leads to an ambiguity problem in which the Z' or ϕ_2 rotation cannot be determined from the SRAS data. It is noted from Collins' dissertation [32] that the α-lath normal corresponds to the $[10\bar{1}0]$ direction in α-phase hcp titanium.

This gave rise to the idea to directly recover the ϕ_2 rotation from an optical image, the sample would need to be etched, but if the SRAS imaging plane and the optical imaging plane are close enough, the 3rd angle might be inferred.

Euler angle recovery – Proof of Concept

An EBSD dataset was collected at the Sensitive Instrument Facility from a β-annealed specimen of Ti-6Al-4V. This specimen was chosen specifically for its very large colony size (~300μm). A 250x173 grid corresponding to a 200nm step size was collected on a FEI Teneo SEM equipped with an Oxford Instruments NordlysMax EBSD detector and CCD. A combination of AZtec, CHANNEL5, TANGO, MTEX-toolkit and

TSL OIM was used for data post processing and visualization of the EBSD data. The site was selected such that there were several large colonies with different orientations in the frame. A 4K resolution Z-contrast backscatter image was taken of the site prior to tilting to stand in for an etched optical image. During the tilt to 70°, the specimen was kept at the stage Eucentric height to minimize spatial error. A forward scatter image was taken in addition to the EBSD dataset and a scratch on the surface provided a fiducial marker that indicated the EBSD frame had shifted and rotated relative to the BSE image. While this was corrected for using a mutual information approach as described in [33], it did lead to some loss of information. As a collaborative effort [34], the solution for ϕ_2 was solved both using the rotation matrices and a geometric approach. The latter approach is presented.

Figure 6.2 shows a schematic of an α-lath normal image. If α-lath normal is viewable we assume that the (0001) can be rotated back into coaxial alignment with the unit normal n by Φ. Φ can be decomposed into two separate rotations, here labeled θ_1 and θ_2.

Inverting this, it can be visualized as a pyramid as shown in Figure 6.3. From this the projection of the ϕ_2 rotation can be backed out and solved for.

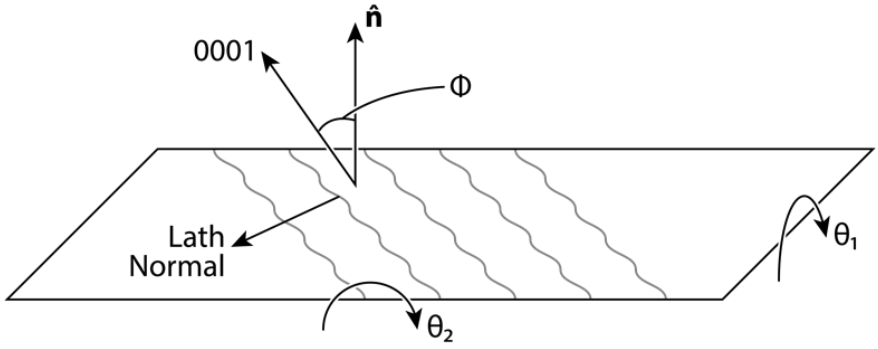

Figure 6.2: Schematic showing an image of an a-lath normal and its relationship to the 0001.

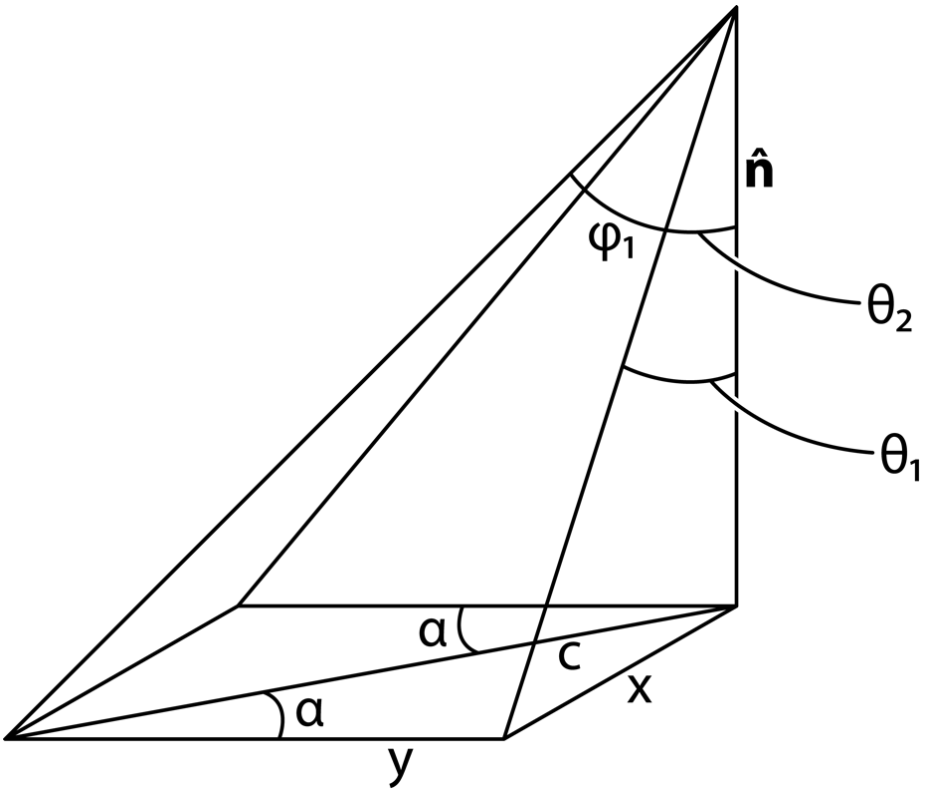

Figure 6.3: Pyramid representation of the lath normal.

$$\cos\theta_2 = \frac{1}{\sqrt{1+(\tan\Phi\cos\phi_1)^2}}; \cos\theta_1 = \frac{1}{\sqrt{1+(\tan\Phi\sin\phi_1)^2}} \qquad \text{Eq. 6.1}$$

$$\phi_2 = \tan^{-1}\frac{\sin(\theta_l \pm \Delta\theta^{10\bar{1}0})\cos\theta_1}{\cos(\theta_l \pm \Delta\theta^{10\bar{1}0})\cos\theta_2} \qquad \text{Eq. 6.2}$$

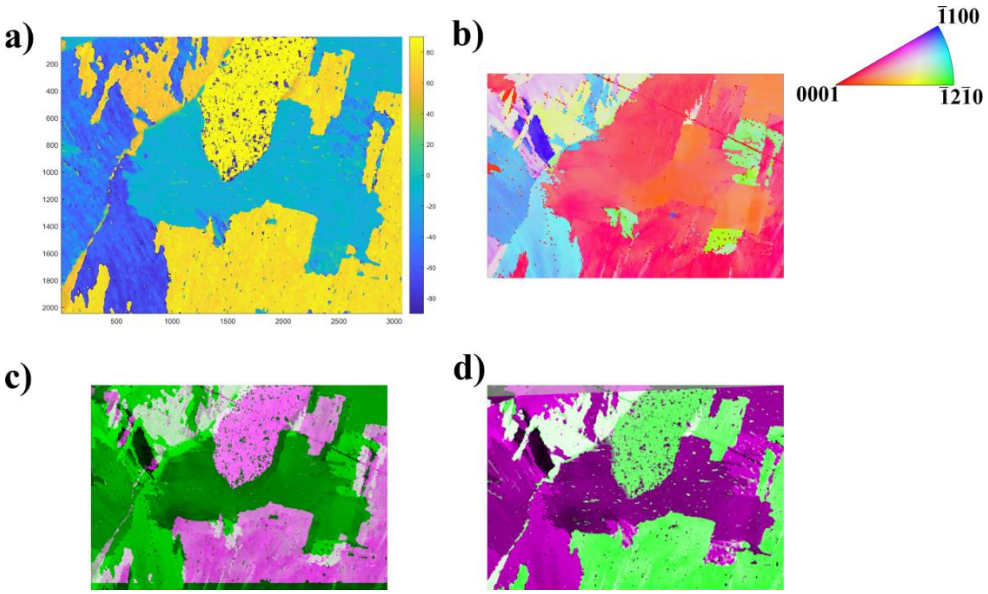

Figure 6.4: Overview of the registration method. a) Normal map computed from MIPAR pattern map. b) EBSD orientation map. c) Pre-registration overlay. d) Post-registration transformed overlay.

The lath orientation map was acquired using the Pattern Mapping functionality in MIPAR, using the Two-Point Correlation method, Window Size setting of 20px, and a Speed parameter of 1 on the original resolution Z-contrast image. To convert this lath map into a lath normal map, 90 degrees were added to each point in the map. The map was then downsampled using MATLAB's built in `imresize()` function to match the width of the EBSD map. The ϕ_1 channel of the EBSD map was used as the basis for the affine transform optimization, using MATLAB's `MattesMutualInformation` object to achieve the result described in [33]. The affine transform that was determined to be optimal was then used to distort the normal map so that the reference frame matched the EBSD data's reference frame.

MTEX was then used to process the EBSD data and integrate it into the MATLAB code. MTEX is a freely-available toolbox for MATLAB that is designed for processing and visualizing EBSD data. A MATLAB script was written to strip out the ϕ_2 angle, leaving only the ϕ_1 and Φ rotations, similar to data that would be present in a SRAS scan. These two angles were then used as inputs along with the normal map to determine what the ϕ_2 should be, based on the observed ϕ_1, Φ and α-lath normal angles for each correlated pixel that was present in the two datasets.

The ϕ_2 angle was collapsed to the interval [0, $\pi/3$] instead of the standard interval of [0, 2π] as it is hypothesized that at this stage there is an ambiguity regarding which a_1 axis corresponds to the actual $[10\bar{1}0]$ direction indicated by the lath normal.

Preliminary Results of the Proof of Concept

Shown in the figure below is the original ϕ_2 as reported in the EBSD dataset. It has been collapsed into the 60° space for comparison with the fused results. In this collapsed mode, there still exists an ambiguity on the correction angle required to bring the various reference frames into alignment and correct for the uncertainty between the visible lath normal and the actual $[10\bar{1}0]$ direction.

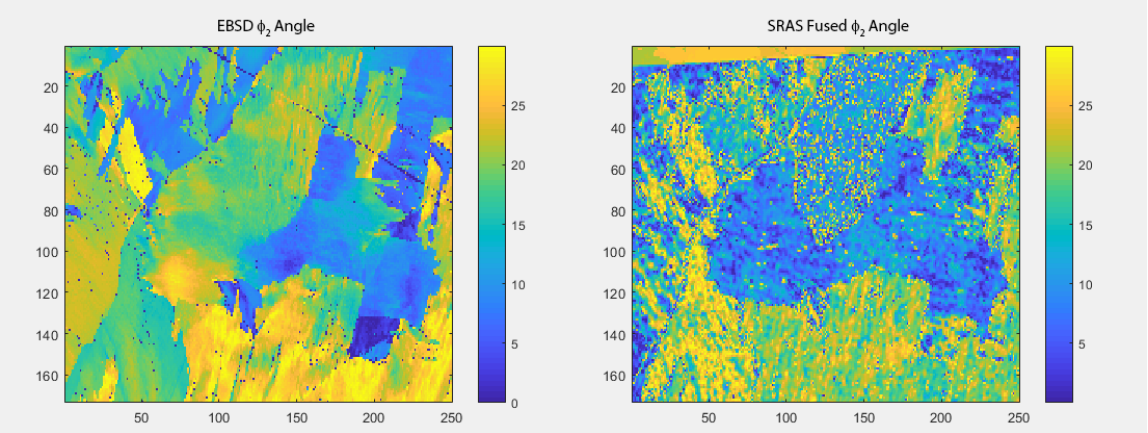

Figure 6.5: Comparision of the original Phi2 rotation in 60-degree space (L) with the SRAS-fused estimation of Phi2 (R)

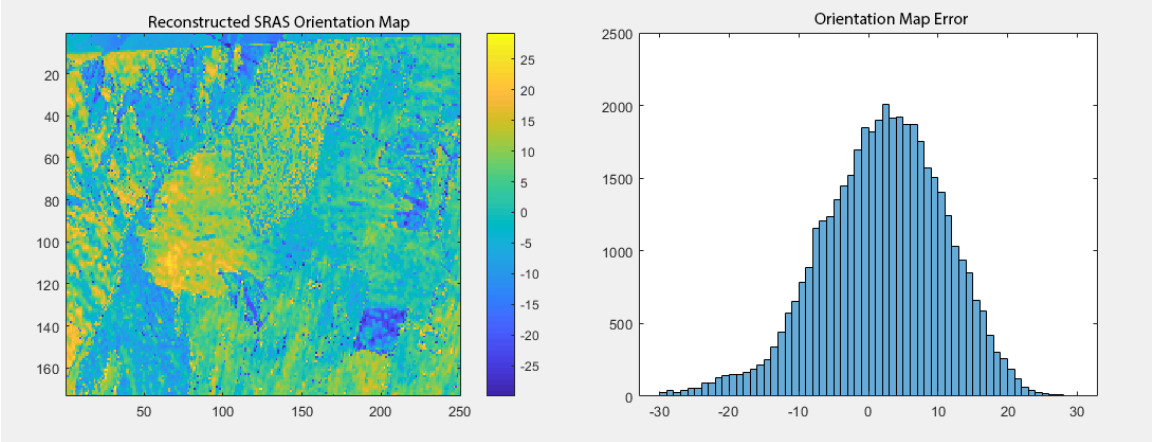

Figure 6.6: SRAS Orientation map reconstructed from the ϕ_1, Φ and lath normal angle. An 8 degree rotation offset has been applied to minimize error.

The compacted results, while not an exact replication of the EBSD dataset do provide validity to the hypothesis that the 3rd angle is recoverable, to a degree, using fusion techniques although refinements to the method need to occur before the technique can progress beyond the research stage. Compounding the problem is the nature of the α-lath interface present in Ti-6Al-4V, it is not as coherent and can deviate by 5 degrees compared to an α-lath interface in Ti-550 for example or another titanium-based alloy with more coherent interfaces.

Future Work

Although more work is required for SRAS to become a drop-in replacement for EBSD, there is promise in some of the methods demonstrated above. Work is currently proceeding to integrate SRAS into a Robomet.3D.

The Robomet.3D is a serial sectioning machine manufactured by United Energy Systems (UES) Inc., and allows for 3-dimensional reconstruction of materials through the

serial sectioning method. The equipment is also outfitted with a Zeiss AxioObserver microscope, providing a stable optical platform that is ideal for the final stage of the integrated SRAS system. Care needs to be taken in selection of the final objective for use in the microscope, as the presence of polymer-based lens elements within objectives could lead to damage or destruction of the objective due to the high energies that will be present in the laser system.

It is envisioned that the SRAS system would utilize the side-entry port of the AxioObserver in conjunction with the standard imaging CCD. The use of a switching mirror would be required to allow for the CCD and the SRAS optical train to share the entry port.

There would be an extra step inside the Robomet.3D's sectioning recipe that would engage the SRAS system and allow for collection of the material orientation prior to etching. This would enable texture investigation and orientation microscopy as a meter-length scale and above.

The resolution of texture, and the ability to determine the distribution of various directions within an additively-manufactured build would further to help the accuracy of the phenomenological equation developed by Collins. By being able to directly sample a build, the AxisDebit term could be removed, and the appropriate direction and orientation specific values could be used for the various contributing mechanisms based on observed distributions of orientations and directions within a given build geometry.

CHAPTER 7. PRELIMINARY RESULTS OF THE APPLICATION OF CHEMICAL AND PROCESS MODELS TO PROBABILISTICALLY PREDICT σ_{YS} IN TI-6AL-4V

Post-Processing Workflow

Shown in Figure 7.1 is the flowchart for how the model presently fuses the data from various sources. The ABAQUS model is used to generate the thermal profiles for the virtual tensiles. These thermal profiles are then fed into several Python scripts to determine the aluminum loss. Oxygen is not included in this model as the agreement between predicted and actual chemistries is currently poor.

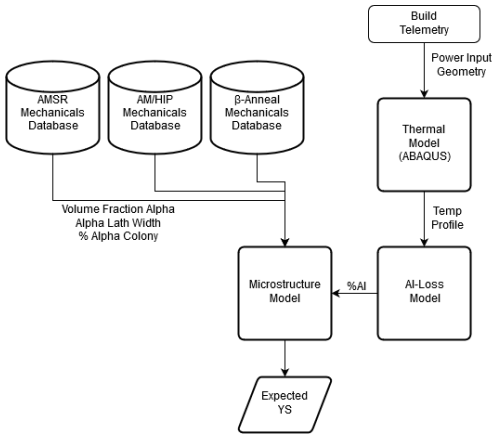

Figure 7.1: Flowchart describing how the various portions of the post-process model.

A hypothesis for this is presented in a later section, and oxygen values are presently modelled as a random selection from a normal distribution based on which heat treatment the tensile has been assigned.

Experimental Dataset

The experimental datasets for the thinwall and thickwall geometries have been pulled from a database built for prior research [2]. Forty samples were classified as a thinwall geometry, which for this experiment was defined as a rib consisting of a single bead, unlike the simulation, these samples had different interlayer rest times. The

thickwall section consists of 103 samples across the three heat treatments mentioned earlier. For this purpose, a thickwall geometry was defined as a rib section consisting of at least three bead widths, these thickwall sections also had varying interlayer rest times. All builds used the same starting stock and roughly the same build process conditions.

Initial Simulated Dataset

The initial dataset was built using the equation developed by Hayes, et. al. [2], although this is a continuation and refinement of work began by Collins, et. al. [5]. A schematic form of the equation, with the particular weights for Ti-6Al-4V is given below in Eqns. 19-25 to illustrate each component's contribution to the overall strength of the material system:

$$\sigma_{YS} = \left(\sigma_0 + \sigma_{SSS} + \sigma_{HP(\alpha-lath)} + \sigma_{HP(\alpha-colony)} + \sigma_{TH} + \sigma_{axisDebit}\right) \quad \text{Eq. 7.1}$$

$$\sigma_0 = F_V^{\alpha} \cdot 89 + F_V^{\beta} \cdot 45 \quad \text{Eq. 7.2}$$

$$\sigma_{SSS} = F_V^{\alpha} \cdot (149 \cdot x_{Al}^{0.667} + 759 \cdot x_O^{0.667}) + F_V^{\beta} \cdot ((22 \cdot x_V^{0.7})^{0.5} + (235 \cdot x_{Fe}^{0.7})^{0.5})^2 \quad \text{Eq. 7.3}$$

$$\sigma_{HP(\alpha-lath)} = F_V^{col} \cdot 150 \cdot (t_{\alpha-lath})^{-0.5} \cdot \left(t_{\beta-rib}\right)^{0.5} \quad \text{Eq. 7.4}$$

$$\sigma_{HP(\alpha-colony)} = F_V^{col} \cdot 125 \cdot \left(t_{colony}\right)^{-0.5} \quad \text{Eq. 7.5}$$

$$\sigma_{TH} = F_V^{BW} \alpha M G b \sqrt{\rho} \quad \text{Eq. 7.6}$$

$$\sigma_{axisDebit} = axisDebit \cdot (\sigma_0 + \sigma_{SSS} + \sigma_{HP(\alpha-lath)} + \sigma_{HP(\alpha-colony)} + \sigma_{TH}) \quad \text{Eq. 7.7}$$

As the process model requires several inputs that were not available at the time of writing, the required missing inputs were sampled as a normal distribution using typical values from each heat treatment database, those defaults are listed in the table below.

Table 7.1: Inputs for the model taken from [2] unless noted. Deviation is given as the percentage of the value.

	AM-SR	AM-HIP	AM-Beta	COV_{SR}	COV_{HIP}	COV_{Beta}
%wt V	4.23%	4.01%	3.91%	3.5%	3.5%	3.5%
%wt Fe	0.171%	0.172%	0.171%	3.5%	3.5%	3.5%
%wt O	0.166%	0.167%	0.166%	3.5%	3.5%	3.5%
F_V α	90.08%	92.60%	90.96%	3.0%	3.0%	3.0%
α-lath thickness	1.099μm	3.533μm	0.998μm	12.5%	12.5%	12.5%
CSF	7.11μm	12.41μm	240μm	N/A	N/A	N/A
F_V Colony	17.80%	19.37%	100%	10.0%	10.0%	0.0%
AxisDebit [35]	x: -4% y: -3% z: -8%	x: -1% y: -2% z: -4%	x: -3.5% y: -2% z: -3.5%	N/A	N/A	N/A

Addition of the Monte Carlo Method

In order to generate the probability curves the Monte Carlo method is used, which arguably has one of the best backstories for any scientific method. Ulam named the method after a relative who had a bit of a gambling problem at the Monte Carlo casino and would often pester relatives for money to fund his habit [36].

By creating normal distributions of what the possible predicted outputs could be depending on test error and uncertainty, an amplification effect can be used to determine what the population distribution might look like compared to the sample distribution.

These distributions were used to generate 10,000 permutations of each datapoint based on observed uncertainties when doing the initial characterization work. Vanadium, oxygen and iron were varied within the known uncertainty of the EDS spectra that were acquired and were set to the averages for each heat treatment as reported in [2]. Similarly, the microstructural features present in each heat treatment such as the alpha lath thickness, volume fraction of the alpha phase, volume fraction of the alpha colonies, were varied according to the observed uncertainties and average values. With these, the probability distributions can be computed and assessed.

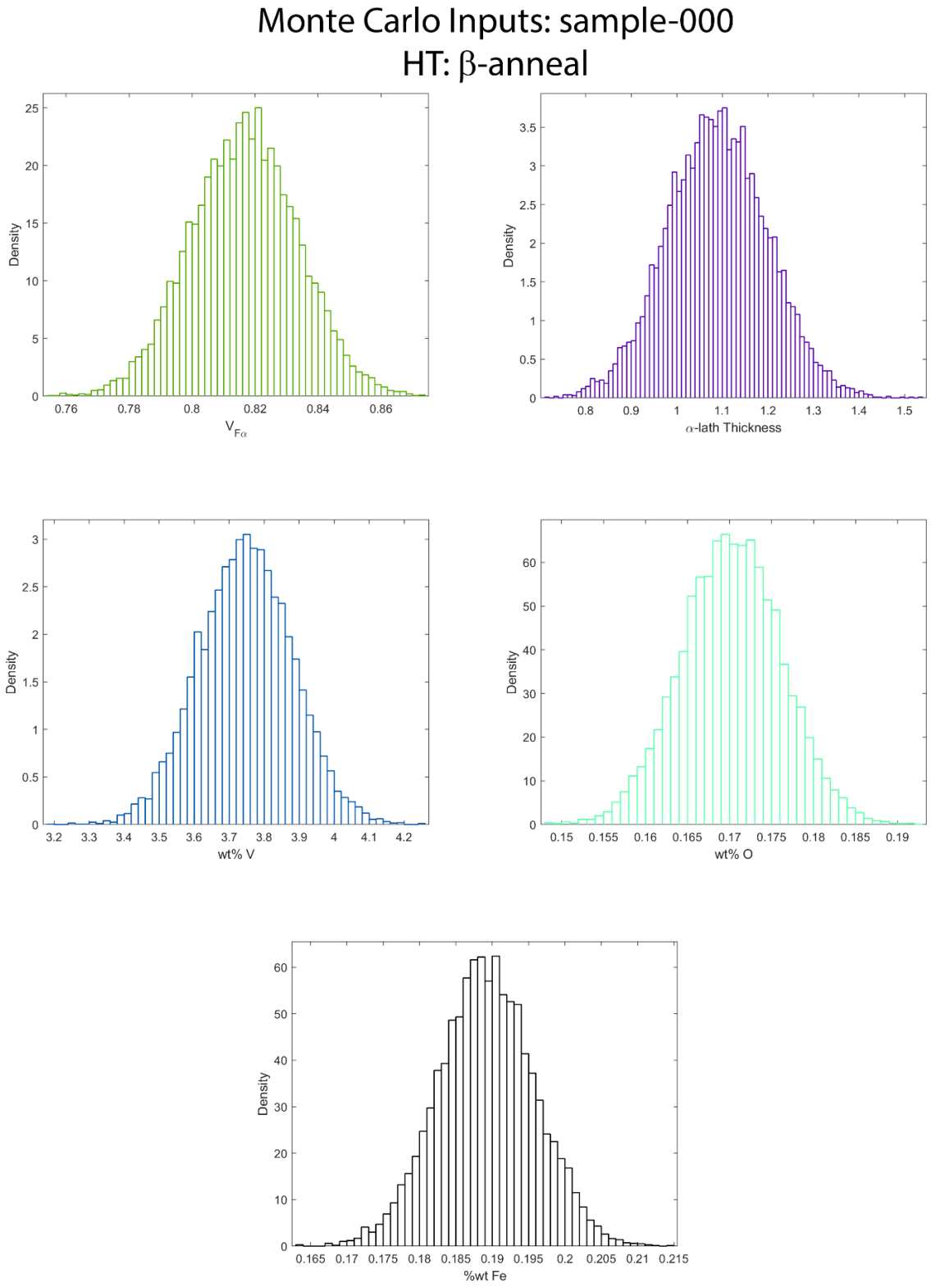

Figure 7.2: Probability Density Distributions (PDPs) for sample-000 assigned to the β-Anneal heat treatment.

Thinwall Calibration Results

The thinwall section was used to calibrate the Langmuir model surface area to volume ratio for the finite element. The probability density function fits are shown in Figure 7.3. After calibration, the model has an average yield strength of 818MPa, with a standard deviation of 75MPa, the experimental dataset reports an average yield strength of 854MPa and standard deviation of 24MPa. There is a 4.2% disagreement in mean values between the experimental and computational datasets. Figure 7.3 shows the cumulative distribution for the experimental and computational datasets. Table 7.2: Thinwall experimental dataset statistics, separated by heat treatment.shows the thinwall results by individual heat treatment, along with the percentage of the dataset the heat treatment makes up.

Table 7.2: Thinwall experimental dataset statistics, separated by heat treatment.

Heat Treatment	$\overline{\sigma_{YS}}$	$\sigma_{\sigma_{YS}}$	Percentage of Dataset
AM-SR	805.4	47.5	50%
AM-β-Anneal	768.9	19.4	16.6%
AM-HIP	760.7	20.1	33.3%

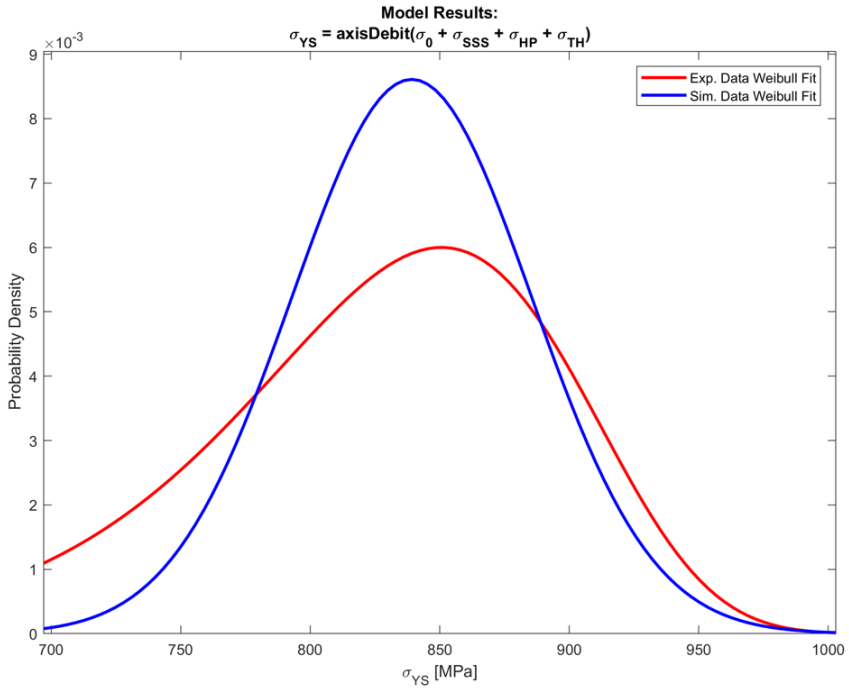

Figure 7.3: Probability density fit for the thinwall after calibration.

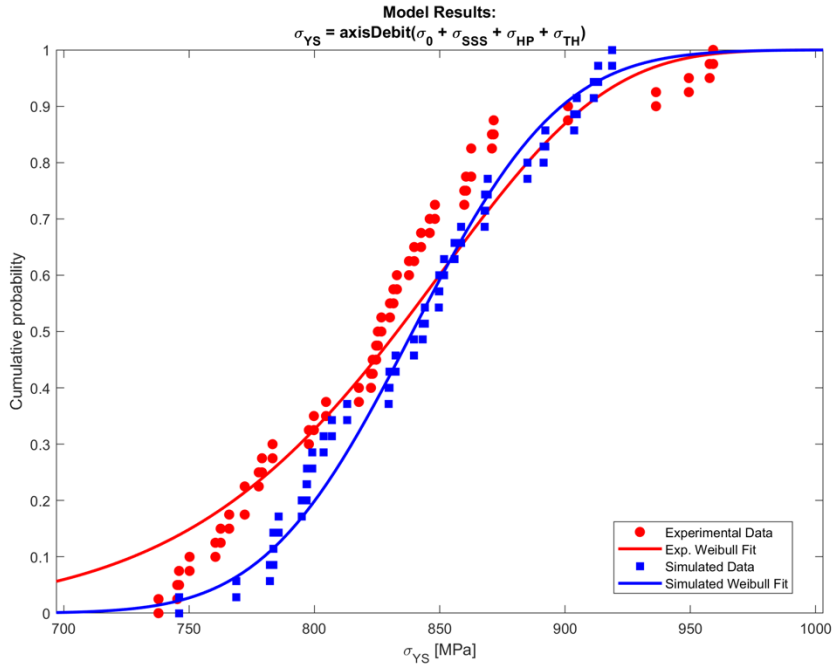

Figure 7.4: Cumulative distribution plot for the thinwall dataset, post-calibration.

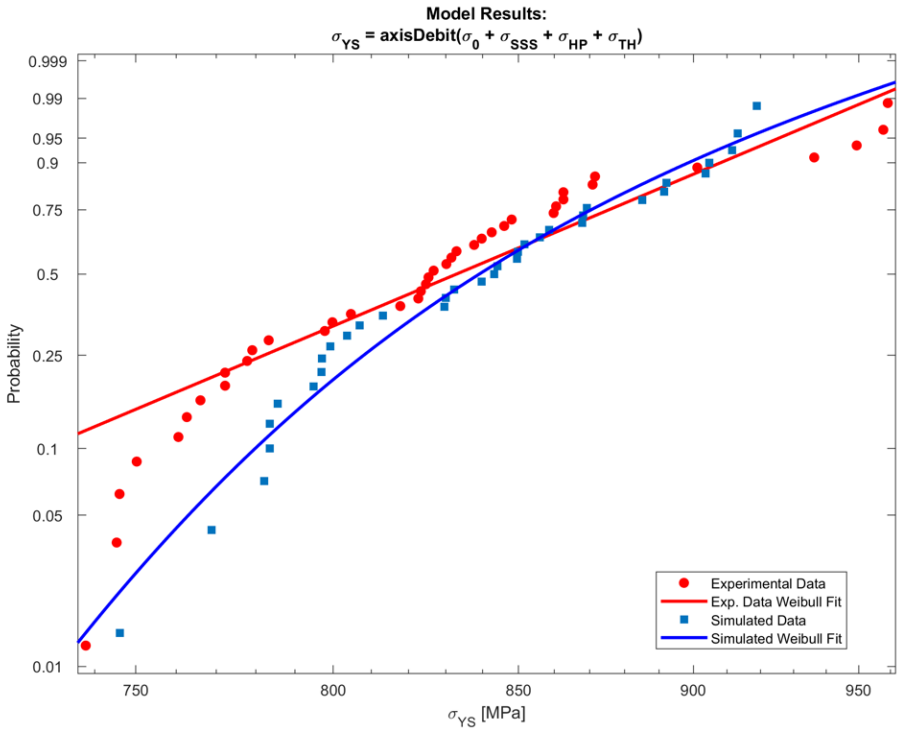

Figure 7.5: Weibull probability plot for thinwall model, post-calibration.

Thickwall Verification Results

After the thinwall results had been calibrated to satisfaction, verification was performed against the portions of the database that would classify as a "thickwall" section. The larger number of samples in this portion of the database allowed for separation of the heat treatments and the results are presented as such. First the AM-SR model will be presented, followed by the AM-β-Anneal and AM-HIP models, the other difference between these results and the results of the previous section is the Monte Carlo procedures have been added to generate a larger sampling distribution. While matching the average yield strength for a thickwall component well, the distributions are not an ideal match.

Table 7.3: Comparison of Average σ_{YS} between model and experimental results.

Treatment	Sim. YS Average	Sim. YS Std. Deviation	Exp. YS Average	Exp. YS Std. Deviation	Error in Avg YS
AM-SR	886	31	856	57	3.5%
AM-HIP	802	28	775	24	3.4%
AM-β-Anneal	780	31	801	27	2.6%

Compared to the experimental results, the model tends to over predict the stress relieved and HIP condition heat treatments, while under predicting the β-Anneal treatment in the current parameter configuration.

There are several things that could be causing the noted discrepancies in the results, one of them is the Monte Carlo sampling of the phase fractions may be causing some of the models to trend low. Further work on integration of physics based modeling for the microstructural features is ongoing. This would better capture the character of the inputs as compared to a sampled distribution. The other contributing factor could be due to mesh artifacts, the meshes for the models presented in this work are reasonably fine, but are missing refinements in areas that many of the boundary conditions operate along and this could be contributing as well.

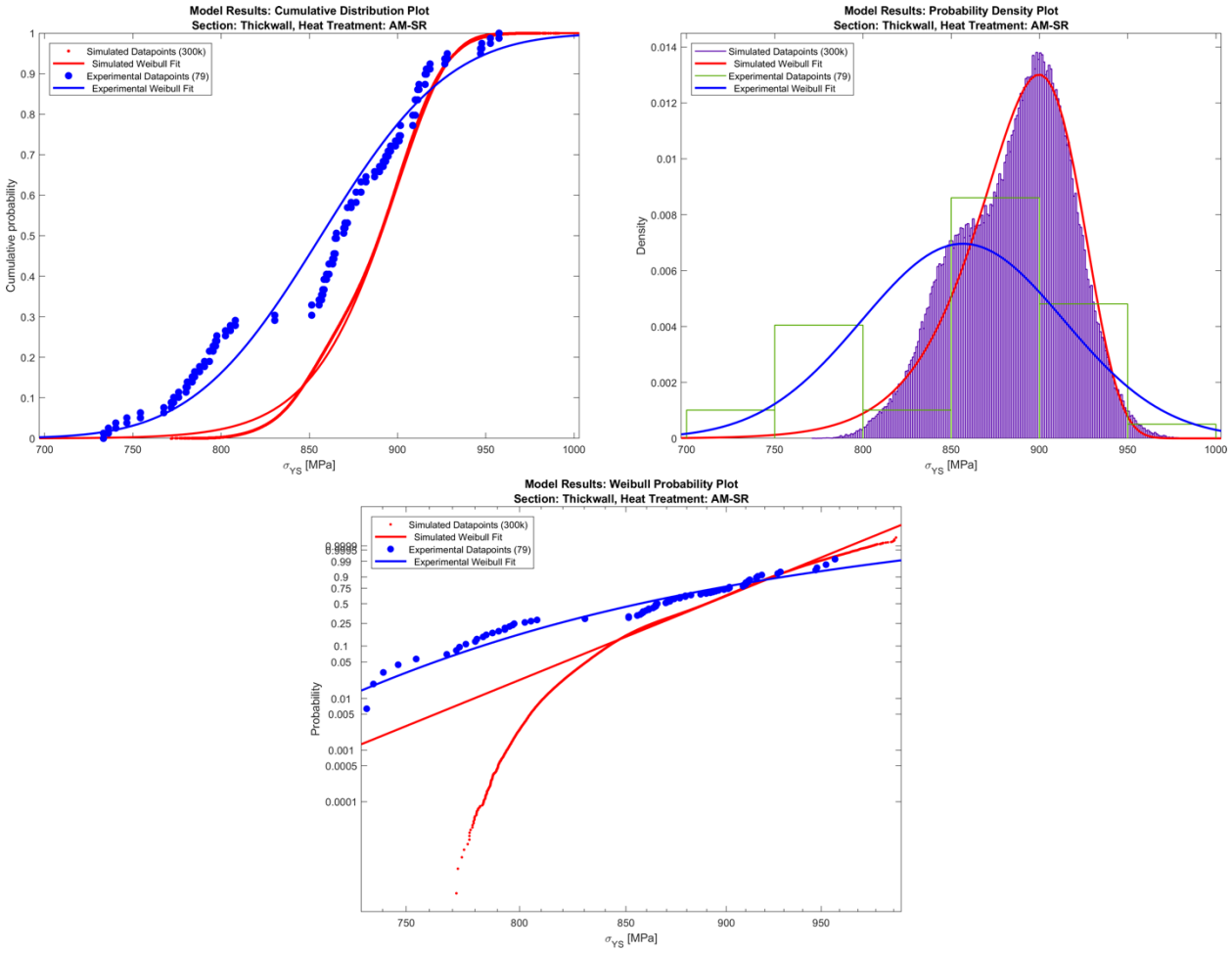

Figure 7.6: Results for the AM-SR heat treat condition. Top-Left: Cumulative distribution. Top-Right: Probability density distribution. Center: Weibull probability plot.

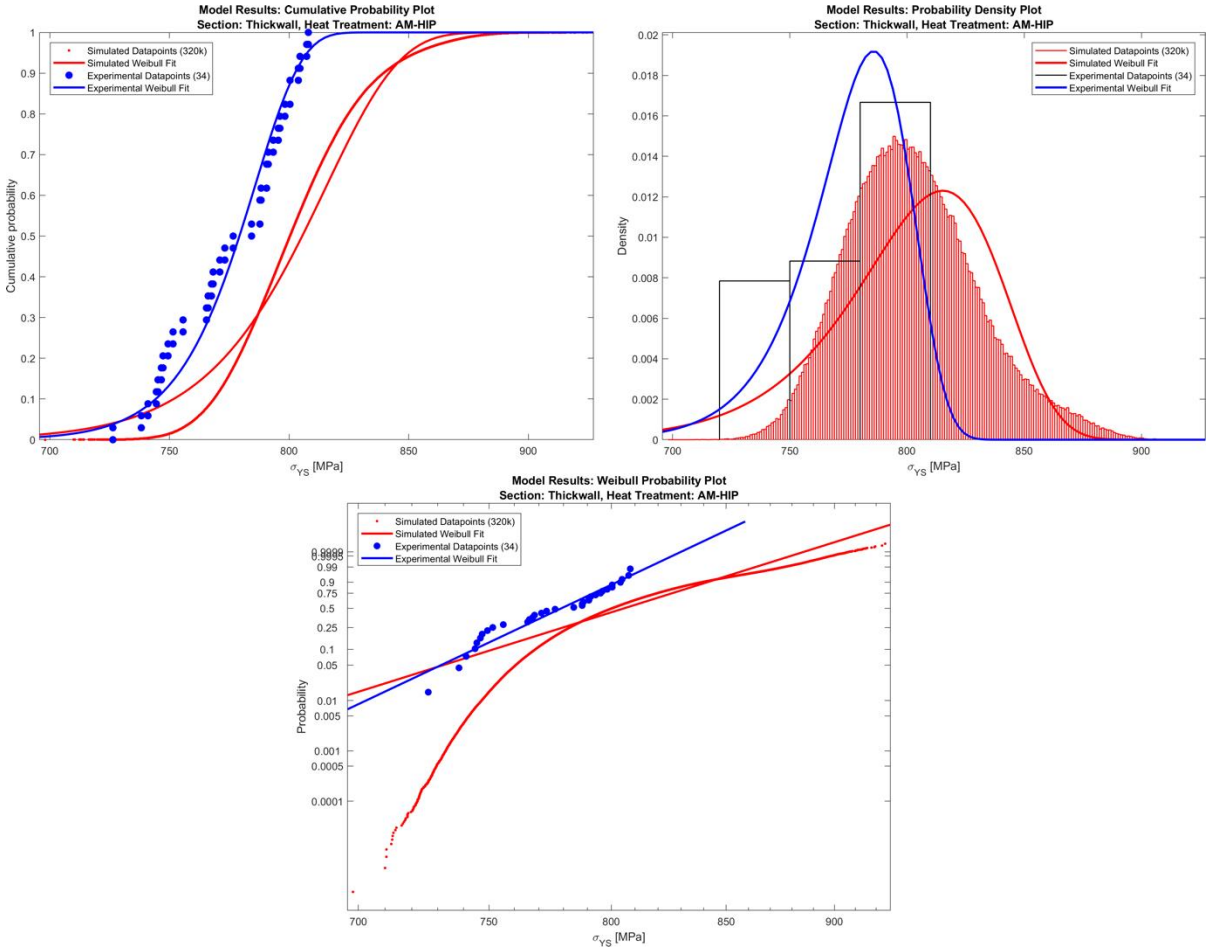

Figure 7.7: Results for the HIP heat treat condition. Top-Left: Cumulative distribution. Top-Right: Probability density function. Center: Weibull probability plot.

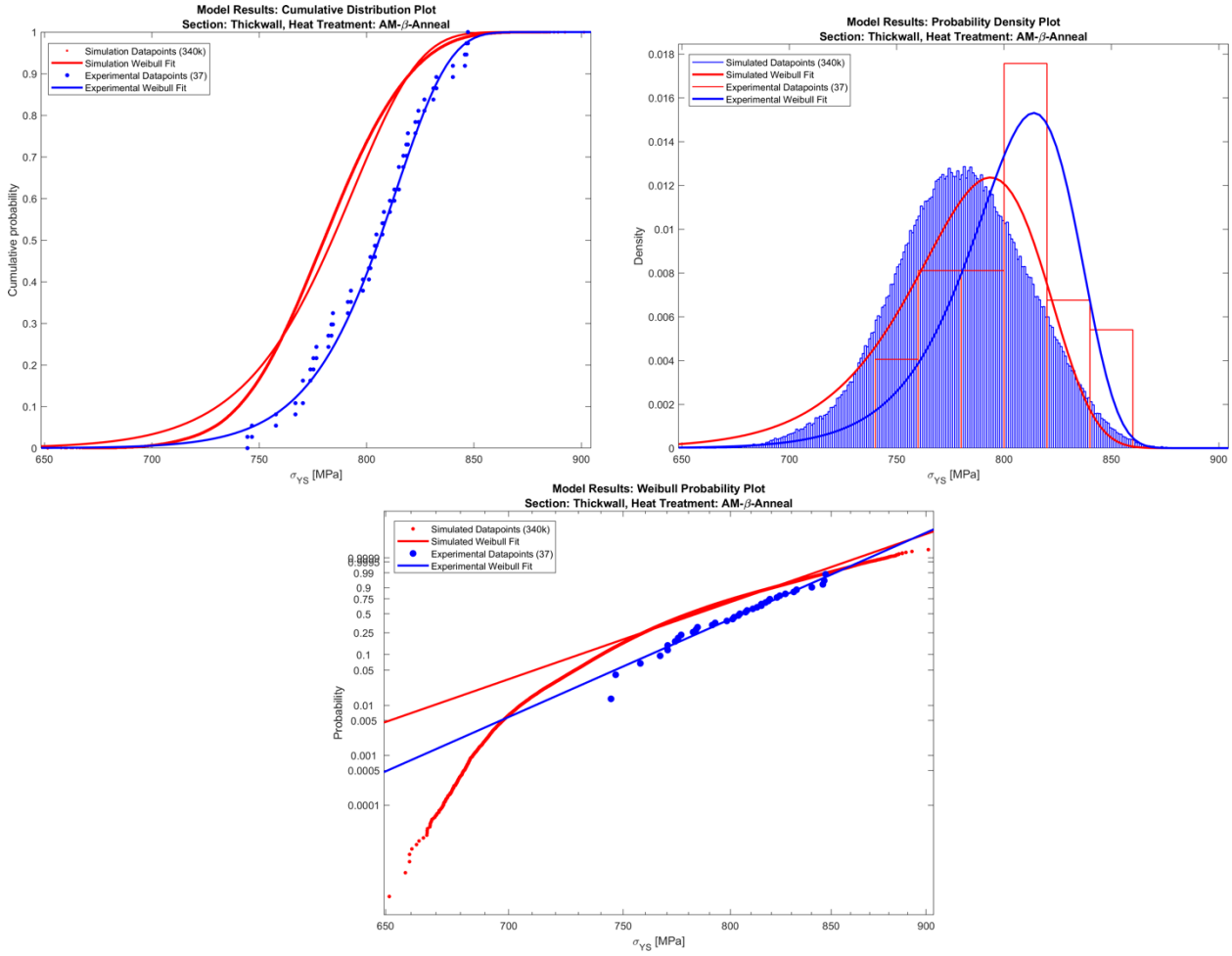

Figure 7.8: Results for the AM-b-Anneal heat treat condition. Top-Left: Cumulative probability distribution. Top-Right: Probability density distribution. Center: Weibull probability plot.

CHAPTER 8. PRINCIPAL ACCOMPLISHMENTS AND FUTURE WORK

Principal Accomplishments

This work has shown that it is possible to do probabilistic modelling of mechanical properties in Titanium-6Al-4V, furthermore it presents a framework or philosophy that can be used outside of any particular FEA package, or with any particular language. The model does not attempt to show itself as an optimized solution, and in fact is a sub optimized one at best, but presents an approach that could be applied to any material system or manufacturing process, provided the groundwork of developing the material databases is done, or if models presently exist that sufficiently describe the process-structure-property-performance relationships.

The work has also shown that it is probable that extraction of the ϕ_2 angle can be done through a combinatorial approach, using known relationships between microstructure and atomic orientation in order to enable orientation microscopy on a scale much larger than what is possible using Electron Backscatter Diffraction or Precession Electron Diffraction techniques, and many of the problems associated with the previously mentioned techniques do not exist with SRAS, which makes the method attractive and worth continued development in the author's opinion.

Future Work

A truly integrated model

Presently, several important variables that could be modeled in sufficient detail are not, notably oxygen content and the volume fraction of the a-phase. It was decided that for this work, oxygen modelling would not be used due to seeing far higher predicted oxygen content in the material than what was experimentally observed. The industrial

partner was contacted for input wire samples, and these samples were sent to Luvak Laboritories for independent testing of chemical content. The wire did not show much difference in content from the final build specimens and this indicated that the fundamental physics of the process were not well understood.

After several discussions between Dr. Collins & Dr. Thuo of ISU, it was hypothesized that if there is an aluminum vapor plume it may be acting like a shield gas. On the Ellingham diagram [37] in Figure 8.1, it is shown that the Al_2O_3 free energy is much lower than the TiO_2 free energy, and it would explain the severe discrepancy between the modelled and observed information.

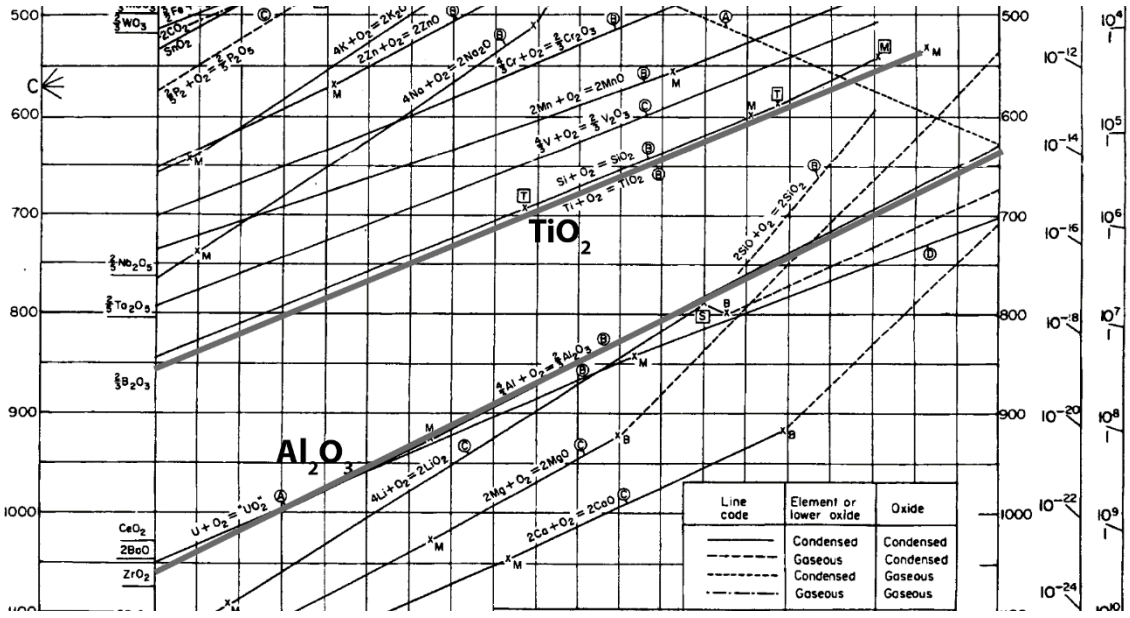

Figure 8.1: Ellingham Diagram for TiO_2 and Al_2O_3

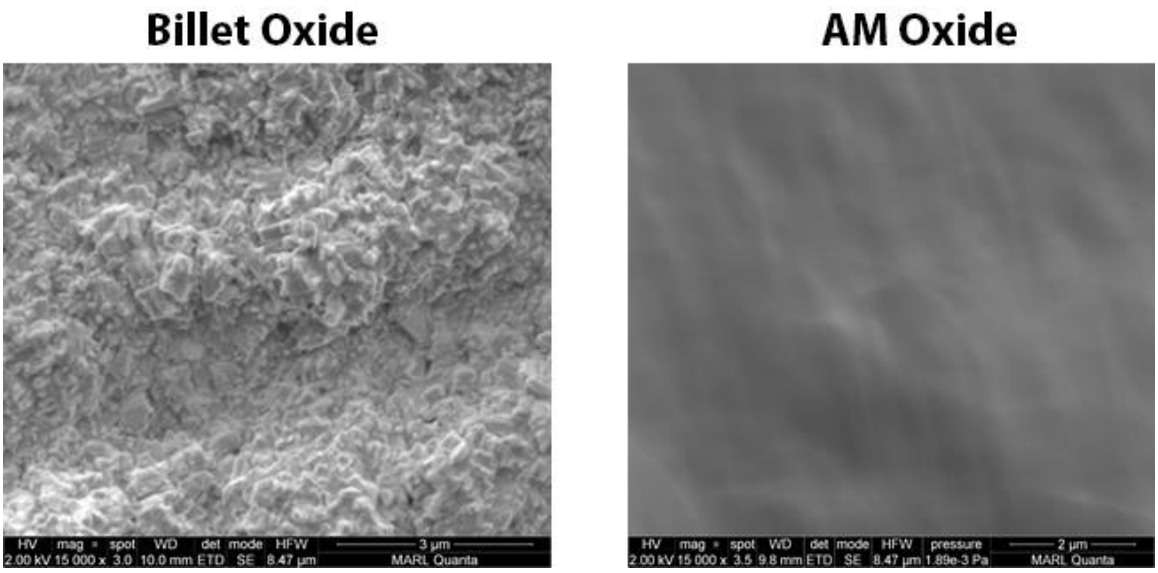

Figure 8.2: Comparison of a small portion of billet oxidized in atmosphere (L), versus the oxide layer on an EBAM build.

There is circumstantial evidence for this phenomenon both in morphology, and chemistry. The surface of a build was inspected under secondary mode at MARL along with a sample that was quickly oxidized in a box furnace at 800C for 1 hour and allowed to air cool. The two surfaces are shown in Figure 8.2. The sample on the left has a typical morphology that would be expected of the native oxide during forging or similar thermomechanical process, however the sample on the right which is from an EBAM build has a very smooth, almost glass-like surface that does not have much deviation. Raman spectroscopy was used to investigate the properties of the oxide layer on the build and shows a mode corresponding to Al_2O_3 bonding, showing that there is a presence of corundum. Although further work is required for confirmation of the formation of corundum, it is a plausible explanation of the discrepancy between the simulated and observed oxygen levels. Further work, perhaps using an in-situ Laser-Induced

Breakdown Spectroscopy (LIBS) system or a similar technique to directly characterize the chemical nature of the vapor plume.

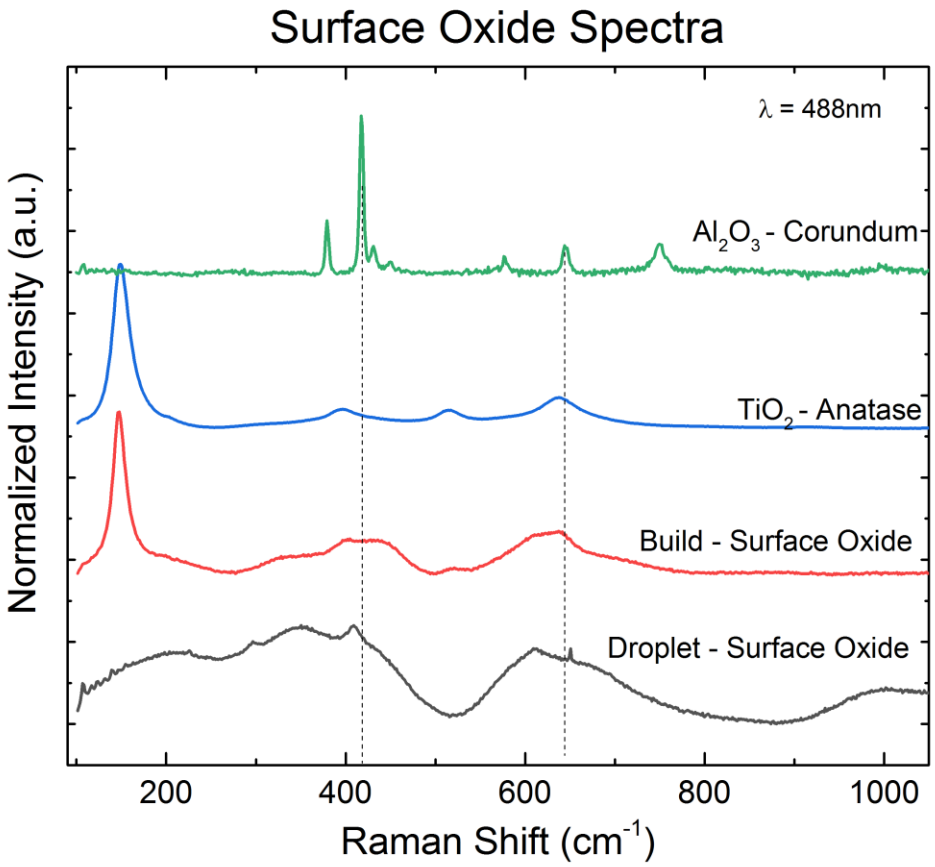

Figure 8.3:Raman spectra captured of a small portion of build. The sample is given in black, while the two standards used for comparison are given in red, and blue.

Raman was an ideal candidate for a quick investigation of the oxide surface character, as metals are invisible to the technique. With the help of Steven Kmiec, an investigation was done on the surface. The green and blue lines in Figure 8.3 represent the spectra that were used as standards. The red line is the response of the surface oxide from the sample that was exposed to a ‘typical’ forging preheat cycle, the black line is the surface oxide of a droplet that was deposited on the substrate near the build. The surface

oxide contains modes centered around 148, 399, 515, and 636 cm^{-1}, corresponding to TiO_2 low-temperature Anatase phase. The primary mode of Al_2O_3 lies at 420cm^{-1}, which corresponds to the discrepancy observed in the droplet, along with the falloff of response between 430-500cm^{-1}, which would imply Anatase is not as present, suggesting higher cooling rates compared to the oxidized sample.

The microstructural characteristics are currently generated through the use of known typical distributions, work by Murgau, Pederson and Lindgren [38] has shown that the Johnson-Mehl, Avrami, & Kolmogorov model can be adapted for the cyclic and varied temperature changes that are seen in the AM build process. This can help provide better and more accurate predictions for the a-fraction as a function of location within the model. Presently in the dataset, the Colony Scale Factor uncertainty is not characterized, leading to assumptions about what distribution and deviation parameters to use.

Utilization of SRAS for Orientation Microscopy

Future work on SRAS will involve the integration of the technique into a serial sectioning system. This would allow for 3-dimensional reconstruction of the orientation relative to the reference frame. The Robomet.3D is ideally suited to this task as all of the mechatronics and control logic have already been tested and proven to be effective for large scale serial sectioning tasks.

Integration work will proceed in several stages, first being the integration of the hardware such as lasers, optical components and mechanical safeties into the Robomet.3D frame. The second stage of integration would require establishing a communication standard between the SRAS computer and the PLC of the Robomet.3D. This can be imagined as another step in the Robomet.3D recipe, which would directly precede the etching step every *n* layers. Then control would need to be passed to the

microscope stage and a timing system would need to be implemented, ideally triggered by the microscope stage itself so that the SRAS system can spatially locate the data that is being acquired.

The microscope will also require modification to the primary and secondary turrets. In the secondary, a right angle mirror is being installed with a narrow-band mirror capable of handling the higher energies that will be produced by the laser system. The primary turret will have the 100x objective replaced with a 20x NIR coated objective, in order to maximize transmission in the 1064μm band, allowing for a lower-power than if the standard epifluor 20x was used. OpticStudio, a commercially available package from Zemax, Inc. is being used to model and develop the laser-train paths and components in order to accurately determine energies that each component will experience.

The Robomet.3D itself also does require some modification for integration of the SRAS system, namely the granite base which the microscope sits on has been enlarged compared to a standard Robomet.3D to accommodate the extra optical and electronic control hardware.

REFERENCES

[1] B. Bensaude-Vincent and A. Hessenbruch, "Materials science: a field about to explode?," *Nature Materials,* vol. 3, pp. 345-347, 2004.

[2] B. J. Hayes, B. W. Martin, B. Welk, S. J. Kuhr, T. K. Ales, D. A. Brice, I. Ghamarian, A. H. Baker, C. V. Haden, D. G. Harlow, H. L. Frasier and P. C. Collins, "Predicting tensile properties of Ti-6Al-4V produced via directed energy deposition," *Acta Materialia,* vol. 133, pp. 120-133, 31 7 2017.

[3] S. Gorsse, C. Hutchingson, M. Gouné and R. Banerjee, "Additive manufacturing of metals: a brief review of the characteristic microstructures and properties of steels, Ti-6Al-4V and high-entropy alloys," *Science and Technology of Advanced Materials,* vol. 18, no. 1, pp. 584-610, 2017.

[4] S. Stecker, K. W. Lachenberg, H. Wang and R. C. Salo, "Advanced electron beam free form fabrication methods & technology," *American Welding Society Conference,* vol. 17, pp. 35-46, Nov 2006.

[5] P. C. Collins, C. V. Haden, I. Ghamarian, B. J. Hayes, T. Ales, G. Penso, V. Dixit and G. Harlow, "Progress Toward an Integration of Process–Structure–Property–Performance Models for “Three-Dimensional (3-D) Printing” of Titanium Alloys," *JOM,* vol. 66, no. 7, pp. 1299-1309, 7 2014.

[6] Sciaky, Inc., "Sciaky Inc.," [Online]. Available: www.sciaky.com. [Accessed 23 3 2018].

[7] T. Wohlers and T. Gornet, "History of Additive Manufacturing," Wohler Associates, 2016.

[8] S. Stecker, "Electron Beam Layer Manufacturing". US Patent 201/061591A1, 16 September 2011.

[9] R. Honig and D. Kramer, Vapor pressure data for the solid and liquid elements, RCA Rev., 1969, p. 285.

[10] A. H. Baker, P. C. Collins and J. C. Williams, "New nomenclatures for additively manufactured titanium alloys," *JOM,* vol. 69, no. 7, pp. 1221-1227, 1 7 2017.

[11] ASTM International, "Standard Test Methods for Tension Testing of Metallic Materials," ASTM International, , West Conshohocken, 2014.

[12] P. C. Collins, B. Welk, T. Searles, J. Tiley and H. L. Frasier, "Development of methods for the quantification of microstructural features in α + β-processed α/β titanium alloys," *Materials Science and Engineering: A,* vol. 508, no. 1-2, pp. 174-182, 20 5 2009.

[13] J. Sosa, D. E. Huber, B. Welk and F. L. Hamish, "Development and application of MIPAR™: a novel software package for two- and three-dimensional microstructural characterization," *Integrating Materials and Manufacturing Innovation,* no. 3:10, December 2014.

[14] R. Boyer, G. Welsch and E. W. Collings, Materials Properties Handbook: Titanium Alloys, ASM International, 1994.

[15] D'assault Systemes, Abaqus Theory Guide, D'assault Systems, 2017, p. 2.11.1.

[16] J. Goldak, A. Chakravarti and Bibby Malcom, "A New Finite Element Model for Welding Heat Sources," *Metallurgical Transactions B,* vol. 15B, no. June 1984, pp. 299-306, 1984.

[17] A. Lecoanet, D. G. Ivey and H. Henein, "Simulation of the Temperature Profile During Welding," in *COMSOL Conference*, Boston, 2014.

[18] P. Michaleris, "Modeling metal deposition in heat transfer analyses of additive manufacturing processes," *Finite Elements in Analysis and Design,* vol. 86, pp. 51-60, 2014.

[19] D'Assault Systemes, "Abaqus Theory Guide: 2.11.1: Uncoupled heat transfer analysis," D'Assault Systems.

[20] M. Boivineau, C. Cagran, D. Doytier, V. Eyraud and M. Nadal, "Thermophysical Properties of Solid and Liquid Ti-6Al-4V (TA6V) Alloy," *International Journal of Thermophysics,* vol. 27, no. 2, March 2006.

[21] T. J. Quinn and J. E. Martin, "A radiometric determination of the Stefan-Boltzmann constant and thermodynamic temperatures between -40C and +100C," *Philos. Trans. R. Soc. London Ser. A,* vol. 316, no. 1536, pp. 85-189, 1985.

[22] E. R. Denlinger, J. Irwin and P. Michaleris, "Thermomechanical modeling of additive manufacturing large parts," *Journal of Manufacturing Science and Engineering,* vol. 136, no. 6, p. 061007, 1 12 2014.

[23] I. Langmuir, "The Vapor Pressure of Metallic Tungsten," *The Physical Review,* vol. 2, no. 5, pp. 329-342, 1913.

[24] S. L. Semiatin and P. A. Kobryn, "Microstructure and texture evolution during solidification processing of Ti–6Al–4V," *Journal of Materials Processing Technology,* vol. 135, pp. 330-339, 2003.

[25] P. C. Collins, D. A. Brice, P. Samimi, I. Ghamarian and H. L. Frasier, "Microstructural Control of Additively Manufactured Metallic Materials," *Annual Review of Material Research,* vol. 46, pp. 63-91, 2016.

[26] C. B. Alcock, V. P. Itkin and M. P. Horrigan, "Vapour Pressure of the Metallic Elements," *Canadian Metallurgical Quarterly,* vol. 23, no. 3, pp. 309-313, 1984.

[27] R. A. Dragoset, A. Musgrove, C. W. Clark, W. C. Martin and K. Olsen, "Periodic Table of the Elements," NIST.

[28] M. Clark, S. D. Sharples and M. G. Somekh, "SAW Imaging in Anisotropic Materials," *Review of Progress in Quantatitive Nondestructive Evaluation,* vol. CP509, 2000.

[29] L. Wenqi, Laser Ultrasonic Method for Determination of Crystallographic Orientation of Large Grain Metals by Spatially Resolved Acoustic Spectroscopy (SRAS), Nottingham: University of Nottingham, 2012.

[30] L. Wenqi, T. K. Ales, M. J. Kenney, P. C. Collins, M. Clark and S. D. Sharples, "Unpublished Research," 2017.

[31] S. D. Sharples, L. Wenqi, M. Clark and M. G. Somkeh, "MICROSTRUCTURE IMAGING USING FREQUENCY SPECTRUM SPATIALLY RESOLVED ACOUSTIC SPECTROSCOPY (F-SRAS)," *AIP Conference Proceedings,* vol. 279, p. 1211, 2010.

[32] P. C. Collins, A combinatorial approach to the development of composition-microstructure-property relationships in titanium alloys using directed laser deposition, The Ohio State University, 2004, p. 340.

[33] E. B. Gulsoy, J. P. Simmons and M. De Graef, "Application of joint histogram and mutual information to registration and data fusion problems in serial sectioning microstructure studies," *Scripta Materialia,* vol. 61, pp. 381-4, 2009.

[34] P. C. Collins, T. K. Ales and M. J. Kenney, "Unpublished Research," 03 2018.

[35] P. C. Collins and T. K. Ales, *Private Communication,* 2018.

[36] P. Hoffman, The Man Who Loved Only Numbers: The Story of Paul Erdős and the Search for Mathematical Truth., Hyperion, 1998, pp. 238-9.

[37] T. Gutowski, "Lecture Notes: MIT 2.813: Energy, Materials and Manufacturing," MIT, 2015.

[38] C. C. Murgau, R. Pederson and L. E. Lindgren, "A model for Ti-6Al-4V microstructure evolution for arbitrary temperature changes," *Modelling Simul. Mater. Sci. Eng.*, vol. 20, 2012.

[39] L. D. Harwell, M. L. Griffith, D. Greene and G. A. Pressley, "Energetic Additive Manufacturing Process with Feed Wire". US Patent 6,143,378, 12 May 1998.

[40] Sciaky, Inc, "Metal Additive Manufacturing Systems | EBAM Systems," [Online]. Available: http://www.sciaky.com/additive-manufacturing/metal-additive-manufacturing-systems. [Accessed 3 March 2017].

[41] ASTM International, "F2924: Standard Specification for Additive Manufacturing Titanium-6 Aluminum-4 Vanadium with Powder Bed Fusion," West Conshohocken, 2014.